

# On the correlation between pre-processing workflow and dimensional accuracy of 3D printed parts in high-precision Material Jetting

Karin J. Chen<sup>a,b,\*</sup>, Ahmed Elkaseer<sup>c,d</sup>, Steffen G. Scholz<sup>a,b</sup>, Veit Hagenmeyer<sup>a</sup>

<sup>a</sup> Institute for Automation and Applied Informatics, Karlsruhe Institute of Technology, Hermann-von-Helmholtz-Platz 1, Eggenstein-Leopoldshafen 76344, Germany

<sup>b</sup> Karlsruhe Nano Micro Facility, Karlsruhe Institute of Technology, Hermann-von-Helmholtz-Platz 1, Eggenstein-Leopoldshafen 76344, Germany

<sup>c</sup> Department of Production Engineering and Mechanical Design, Faculty of Engineering, Port Said University, Port Fuad 42526, Egypt

<sup>d</sup> Department of Mechanical Engineering, Faculty of Engineering, The British University in Egypt (BUE), El-Sherouk City 11837, Egypt

## ARTICLE INFO

### Keywords:

Material Jetting  
Additive manufacturing  
Dimensional accuracy  
High-precision  
AM workflow

## ABSTRACT

Material Jetting (MJ) is distinguished in the additive manufacturing field for its ability to create accurate multi-material functional objects with features in the range of few micrometers. Analyzing the impact of each step in MJ from virtual design to 3D printed object on the process response is essential for optimizing the technology's capabilities. The current state-of-the-art reveals a gap in MJ regarding the fundamental understanding of the correlation between the pre-processing workflow and the geometrical and dimensional accuracy. This study aims to bridge this gap by examining factors such as utilization of different CAD software with diverse working principles, part-based versus assembly-based design, alternative 3D model formats (STL, OBJ, 3MF, AMF, STP), and slicing approaches (using open-source slicers). Two test specimens, each containing ten elements (either cylinders or hemispheres) with diameters ranging from 254  $\mu\text{m}$  to 12.7 mm are examined. The results demonstrate the significant influence of the aforementioned factors on geometrical and dimensional accuracy, except for 3D model formats. Specifically, for large elements, the achievable accuracy depends on the tessellation approach of the CAD system, while for very small elements, the rasterization process is defining, and designing in assembly mode can further enhance accuracy. The handling of the 3D model by the slicer particularly affects geometrical accuracy. Experimental validation confirms the impact of the pre-processing workflow, though the data-related dimensional deviation for the base layer is masked by the wetting behavior of the dispensed droplets on the substrate.

## 1. Introduction

Additive Manufacturing (AM) encompasses a group of manufacturing technologies which generates parts by sequentially adding material layer by layer. This innovative approach of manufacturing offers significant advantages over conventional, subtractive manufacturing methods. The advantages include broad and versatile design possibilities, sustainable and selective applications of material and the creation of complex multi-material components and systems with heterogeneous functional properties [1,2]. According to the most recent ISO standard 52900, AM is categorized into seven groups entailing different technologies. Each of these technologies is distinguished by its unique physical mechanism and material it can process, and the specific accuracy, surface quality and integrity it can achieve

[3]. Material Jetting (MJ), alternative term is 3D inkjet printing, is recognized for its accuracy, capable of producing parts with accuracies down to 10  $\mu\text{m}$  [4], making it suitable for complex functional multi-material applications such as printed electronics [5], optical lenses [6], personalized pharmaceuticals [7], scaffolds for tissue engineering [8], implants [9], and microsystems [10]. MJ deploys the piezo-based inkjet printing technology to generate a single layer by depositing thousands of droplets simultaneously through numerous nozzles, each equipped with a piezo actuator. These actuators deform in response to an electrical signal, known as waveform, generating a pressure wave in the nozzle channel that ejects material from the nozzle. Currently, commercially available piezo-based printheads can print droplet volumes from 1 pl up to about 100 pl per nozzle, allowing for precisions in the single- and double-digits micrometer range within the

\* Corresponding author at: Institute for Automation and Applied Informatics, Karlsruhe Institute of Technology, Hermann-von-Helmholtz-Platz 1, Eggenstein-Leopoldshafen 76344, Germany.

E-mail address: [karin.chen@kit.edu](mailto:karin.chen@kit.edu) (K.J. Chen).

<https://doi.org/10.1016/j.addma.2024.104335>

Received 30 April 2024; Received in revised form 12 July 2024; Accepted 31 July 2024

Available online 5 August 2024

2214-8604/© 2024 The Author(s). Published by Elsevier B.V. This is an open access article under the CC BY license (<http://creativecommons.org/licenses/by/4.0/>).

printing plane. Various types of materials from solvent-based to UV-curable ink can be processed [11], the latter one being the most common material used for 3D printing. Once a single layer has been entirely printed, the layer undergoes a curing step using a UV source which solidifies the wet printed layer. During this curing process, the polymer chains in the ink form an irreversible polymer network [12]. These two steps, printing and curing, are repeated for every layer until the 3D object is completed. To ensure consistent layer thickness, some commercial printers mechanically smoothen and remove excessive materials from the printed layer immediately after printing and before curing [13].

The 3D printing process starts with the design of the virtual model, serving as the foundation for the entire AM workflow. This workflow transforms the virtual 3D model into a physical object through multiple steps, which vary slightly depending on the specific AM technology employed. For instances, Material Extrusion requires a .gcode file to control the motion of the nozzle and the position for material deposition [14]. Meanwhile, for the photopolymer-based AM technologies, e.g. Vat Photopolymerization (VP) and MJ, the pattern to be printed for each layer is based on binary raster images. The focus of the present study will be on the 3D printing workflow specific to MJ.

The established workflow for generating 3D printed objects from a virtual (CAD) model comprises six steps (Fig. 1): (I) Designing the virtual model using CAD software; (II) Transforming the proprietary CAD model into an interoperable 3D model format (such as the STL format); (III) Slicing the interoperable 3D model along the print direction into layers represented by raster images. If necessary, support structures may be added before or after the slicing step [15]. In addition to the layer image data, some slicers generate machine information and process parameters as well, defining conditions for curing, printing, chuck increments, etc. during the manufacturing process [16]. The fourth phase (IV) refers to the actual printing process, and the final phase (V) accounts for the post-processing activities for finishing the printed part. The phases (I) to (III) are termed as pre-processing workflow which is considered of interest in the present study.

It is worth stating that MJ offers significant potential for fabricating

precise and complex objects within the micrometer size range. A thorough understanding of how each phase in the pre-processing workflow affects the dimensional accuracy is crucial for achieving high-precision and high-accuracy outcomes in various applications. Therefore, the present paper aims to explore the impact of pre-processing steps within the MJ workflow on geometrical and dimensional deviation. These findings will be experimentally validated through the printing of curved specimens, thereby contributing valuable insights into the optimization of MJ process for enhanced accuracy.

The remainder of the paper is structured as follows: First, a state-of-the-art of the influence of individual phases in the workflow of polymer-based AM on the resulting dimensional and geometrical deviation of the printed object is given in Section 2, followed by a description of the materials and methodologies deployed in this study (Section 3), including the test specimens' design, printing and experimental characterization settings. Section 4, in which the results are illustrated and discussed, is subdivided into three subsections - the influence of the conversion process from CAD model to a tessellated interoperable 3D model format (Section 4.1), the relationship between slicer software and resulting dimensional and geometrical accuracy (Section 4.2), and the results of the experimental validation (Section 4.3). In Section 5, the paper is concluded and the future work is addressed.

## 2. State-of-the-art

In the late 1990s, it has been first mentioned that the global deviation present in a 3D printed object - defined as the discrepancy between the nominal object (virtual model) and the actual printed object - can be categorized into errors originating from the slicing process and those from the fabrication process [17]. Deviations related to print data remain confined to the single layer level and do not propagate across layers, while deviations stemming from the printing process do [18]. Data-related error could be correlated to the data acquisition process [19], tessellation resolution [20], slicing software [21] and part design [22]. Deviations induced during the printing process can be influenced by material properties [23], printing process parameters [24], part orientation [25], printer [26] and post-treatment process [25].

Applications that demand high accuracy are particularly prevalent in the medical sector, where they are crucial for creating prosthesis or anatomical models for mock-up trainings before demanding surgeries. Given the critical need for accuracy in these applications, it is not surprising that some of the most comprehensive studies using MJ on the dimensional deviation introduced by individual steps in the AM workflow have been reported for medical 3D printing. For instances, Salmi et al. found a dimensional deviation of  $0.18 \pm 0.12$  % between a medical skull printed with MJ and its original DICOM model [27]. Pinto et al. examined the deviations occurring at different stages of the AM workflow for medical models. However, the resulting deviation stems mostly from voxels only existing in the virtual 3D model but not in the medical 3D printed model. Their analysis also highlighted that the tessellation step has been determined to be a significant factor for the dimensional deviation [20]. Tessellation describes the approach to approximate a 3D model by subdividing the surface into polygon facets, normally triangles, each facet being described by a normal vector and three vertices [28].

Several other studies deploying MJ technology specifically addressed individual phases of the AM workflow. Godec et al. reported that the greatest deviation after tessellation occurs at curved surfaces [29]. Kardel et al. [30] and Khoshkhoo et al. [31] explored the relationship between part thickness and distortion behavior of MJ printed part due to the UV-curing process. While there are general design guidelines for MJ objects, such as wall thickness, smallest possible feature size, etc. [32], recommendations are only valid within the scope of the printer's settings, including its printhead and material capabilities. Hällgren et al. found out that the achievable deviation depends strongly on the selected CAD software [33]. No study on the influence of MJ specific slicer

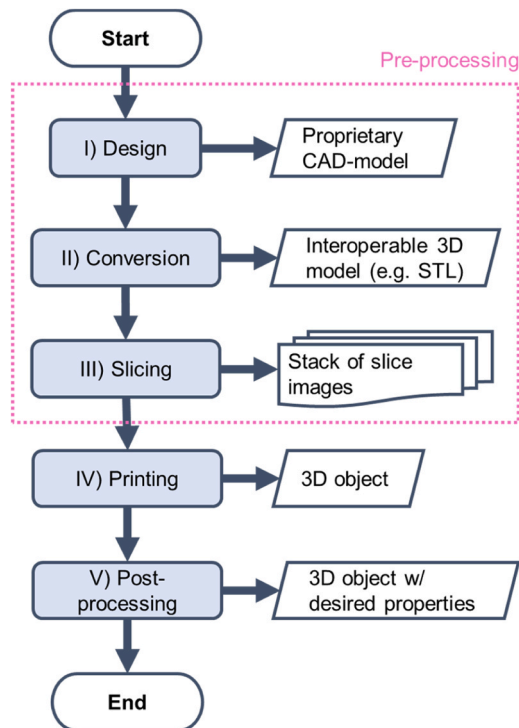


Fig. 1. Workflow of generating a 3D object from a virtual CAD model in Material Jetting.

software on dimensional accuracy has been reported, as the majority of the investigations focuses on material extrusion technology. Multiple studies illuminated how part orientation of the 3D model on the slicer platform impacts the resulting dimensional deviation [34].

In contrast, numerous studies inquired into the correlation between printing parameters/conditions and resulting deviations in MJ. Elkaseer et al. carried out a comprehensive analysis of how print and image parameters, and UV-curing condition influence the layer height [35]. Similarly, Chen et al. identified the interdependence between lateral dimensions of printed objects and UV-curing settings [36]. The broad variety of examined aspects mirrors the large number of parameters governing the quality of the printed objects in MJ. Regarding the influence of post-printing phases on the dimensional accuracy in MJ, Yousef et al. discovered that the dimensional accuracy of MJ specimens alters over time contingent on the storage condition [37].

Apart from the relationship between individual phases of the AM workflow and the dimensional and geometrical deviation, the influence of 3D model formats is yet to be examined. Multiple interoperable 3D formats exist that are commonly used in AM such as STL (Stereolithography or Standard Tessellation Language), OBJ, 3MF (3D Manufacturing Format) and AMF (Additive Manufacturing File Format). The formats are listed in a descending order of popularity [38]. Both STL and 3MF deploy planar triangles to approximate the geometrical shape of the 3D model [39,40], whereby the format 3MF enables additional information about color, texture, metadata and material, etc., to be stored in the file, a development driven by the AM community in order to meet the new trend in AM towards the printing of complex multi-material and colored parts [41]. OBJ can approximate the 3D models either by polygon faces, free-form curves or surfaces [39], or by Non-Uniform Rational B-Spline (NURBS), a much more exact description of the geometry, by utilizing mathematical formulas to define the curves and patches [42]. AMF allows curved triangular facets to be deployed for delineating the geometry of curved objects more accurately [43], discernible with the elements <normal> or <edge> in the AMF file [44]. STP, a well-established non-tessellated standard file format for exchanging technical product data [45], is regarded by some researchers as the best standard for describing 3D model and AM data precisely [46]. There has yet been no experimental validation of the advantages of alternative 3D model formats even though for some of them it is claimed to be more accurate than the format STL [28,43].

The above-conducted literature review clearly shows a gap in comprehensive studies addressing the entire pre-processing workflow in Material Jetting and its impact on the geometrical and dimensional accuracy. For instances, no work examined systematically the model design process within the CAD software environment, particularly regarding aspects such as axis referencing or the design as an assembly model. Furthermore, no systematic investigation into the relationship between specimen size and geometry, and dimensional accuracy has been reported. Most existing studies focus on objects with complex shapes or were carried out on commercial printers that use designated printheads and print settings, limiting the exploration of accuracy.

Hence, this research intends to bridge the identified gaps by systematically examining three pivotal phases of the workflow: a) Design in a CAD software, focusing on the impact of creating designs as part-based or assembly-based model, and the effect of the featured elements' sizes; b) Conversion to an interoperable format, assessing the difference among various 3D model formats; and c) Slicing, evaluating the effects of using three different open-access slicers.

### 3. Materials and methods

In the following, the description of the test specimens is provided. This is followed by the methodology utilized for evaluating dimensional deviation in the print data. Next, the software programs used for both CAD design and slicing are presented. Finally, the relevant parameters of the printing process as well as the characterization procedures for the

experimental validation of the 3D printed parts are reported.

#### 3.1. Test specimens

Test specimens A and B each consist of 10 elements and are designed to investigate how the various factors in the pre-processing workflow, namely the working principles of CAD software, CAD design (part-based vs. assembly-based), data formats, and slicer affect the geometrical and dimensional accuracy of the 3D printed model (Fig. 2). Test specimen A, which is cylinder-based, is specifically designed for assessing the stability of the slicer software along the slice height (Section 4.2). The hemispheres in test specimen B are deployed to investigate the impacts of these aforementioned factors on the geometrical and dimensional deviation of the 3D model across all three dimensions x, y, and z (slice direction), with a particular focus on the generated slice images, and considering the size of the elements (Section 4.1). Test specimen A was not assessed in this part of the study as the results determined for test specimen A are identical to the results of the first layer (base layer) obtained for test specimen B since the base diameters and positions of the elements are identical in both test specimens. The dimensions of the elements in both test specimens range from 0.254 mm (exactly 1/100 in.) to 12.7 mm (exactly 1/2 in.), covering typical dimensions in MJ. Given that resolution is defined as the number of dots per inch (dpi), the size of one pixel is most accurately described when using inches as the unit of design. The corresponding sizes in millimeters are also provided for reference. The total size of each test specimen is 17.85 mm (x-direction) by 19.12 mm (y-direction). Each object is placed at the center of the platform (x=y=12.7 mm), and one specimen is sliced at a time.

#### 3.2. Evaluation of dimensional deviation

The accuracy of the tessellated 3D model is quantified by the difference  $Err_{px}$  between the number of pixels  $Px_{model}$  that is required for representing the cross-section area of the analytical hemisphere model at a particular z-height and the number of pixel  $Px_{sliced}$  that is actually present in the sliced image at this particular z-height (Eq. 1).

$$Err_{px} = Px_{sliced} - Px_{model} [-] \quad (1)$$

In order to obtain  $Px_{model}$ , the following calculations are made: First, the area of the circular cross-section of the analytical model  $A_{model}$  at the height  $z$  of interest (Eq. 2) is determined, with the radius  $r_z$  being calculated according to Eq. 3, where  $r_0$  is the base radius of the hemisphere.

$$A_{model} = \pi * r_z^2 [m^2] \quad (2)$$

$$r_z = \sqrt{(r_0^2 - z^2)} [m] \quad (3)$$

This cross-section area stated in the unit  $[m^2]$  is then converted into the number of pixels  $Px_{model}$  that is needed to represent this area with a specific resolution by dividing the circular area by the area of one pixel  $A_{px}$  and rounded to the next integer number (Eq. 4).

$$Px_{model} = \left\lfloor \frac{\pi * r_0^2}{A_{px}} \right\rfloor [-] \quad (4)$$

The area of one pixel (pixel size)  $A_{px}$  is the square value of  $d$ , the edge length of one pixel which is dependent on the resolution  $R$  (Eq. 5).

$$A_{px} = d^2 = \left( \frac{25400 \mu m}{R} \right)^2 [\mu m^2] \quad (5)$$

Due to the discretization nature of the raster image format, a circle can only be approximated by square pixels. Since the underlying algorithm in the slicer regarding the rasterization of a circle pattern is unknown, thus it is unclear how many pixels are required to represent a circle of a particular size, the approach as shown in Eq. 4 is introduced to

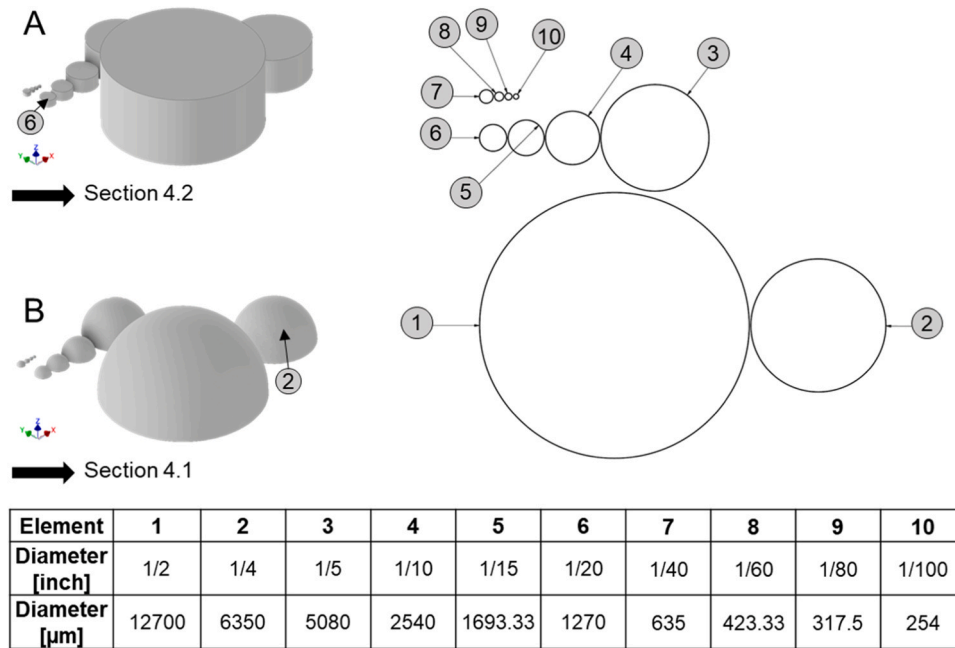


Fig. 2. Test specimens A (cylinders) and B (hemispheres) consisting of 10 elements each (numbering of the elements is indicated in the gray circle).

define a reference value  $Px_{nom}$ . The number of pixels in the slice image  $Px_{image}$ , by contrast, is obtained by retrieving the slice image at the z-height of interest and by counting the number of white pixels using a script written in MATLAB®. The areal deviation is calculated via the difference in number of pixels to reduce the difference between the analytical model, which is a perfectly shaped circle, and the raster slice image. The areal deviation is calculated by multiplying the number of pixels  $Err_{px}$  by the pixel size  $A_{px}$  (Eq. 6). Fig. 3 illustrates the relationship between the equations.

$$Err_{area} = Err_{px} * A_{px} [m^2] \quad (6)$$

### 3.3. Conversion to tessellated 3D model

In additive manufacturing, 3D models are usually tessellated by utilizing triangle facets. The triangulation algorithm can either be directly applied to the 3D surface (direct approach) or indirectly by first generating a 2D parametric mesh that is then mapped onto the 3D surface, or by combining these two approaches [47]. Delaunay triangulation, Advancing Front Technique and Octree-based triangulation algorithm are commonly used triangulation approaches for this purpose [48]. The first two algorithms can be applied in both 2D and 3D space and generates high quality meshes, but is less efficient compared to the latter approach [48]. The mesh density depends on the given approximation tolerance and the maximal edge length of the facet, which the user can define in the STL export settings [48]. The tessellation begins with segmenting the boundary curves of the CAD model into sub-sections which are further sub-divided until the error of each segmented curve section is within the defined approximation tolerance [48].

The CAD software packages Inventor Professional 2023 (Inventor), Solidworks 2022 (Solidworks) and Creo Parametric 4.0 (Creo) and the 3D model data formats AMF, 3MF, STL, OBJ and STP are investigated in this study. Regarding the first two CAD software programs, the export settings and value range do not change when opting for different tessellation 3D model formats (except for STP, which is not a tessellation format). The default accuracy settings for “high-accuracy” are deployed for the export of the tessellated 3D models (Table 1).

The comparison of different 3D model formats is restricted to files exported from the same CAD software to avoid the lack of comparability

of the tessellation settings across different CAD software packages influencing the results. Generally, each CAD model operates with a different software library that utilizes different approaches to describe, visualize and tessellate the 3D model [49]. Solidworks, for instance, uses a commercially available licensed geometrical modelling kernel named Parasolid®, whereas Autodesk Inventor and PTC are using kernels that are developed in-house, namely ShapeManager® (Autodesk Inventor, ACIS based [50]) and Granite (PTC Creo) [51]. Only limited information is publicly available about these kernels. For Parasolid®, it is mentioned that the mesh generation option allows the specification of the minimum and maximum facet width, and curve and surface tolerance, as well as the option to ignore features during the faceting process that are smaller than a certain size [52].

The AMF and 3MF models exported from Solidworks are the only ones that can be sliced on the PRUSASlicer, whilst the same formats exported from Creo prompt an error in the PRUSASlicer upon import. Inventor does not support the formats AMF and 3MF.

The test specimen B is designed as a “part” model and an “assembly” model to assess the impact of these two different CAD design approaches on the dimensional accuracy. In our case, creating the virtual 3D model as a part object means that all ten elements are designed in one “part” file, while in the assembly mode, each element of the model is first designed as individual parts (multiple part files) and then assembled in an “assembly” file. Assembly-based design is required for instance for multi-material parts, where each element could be assigned to a specific material. In Inventor and Solidworks, the tessellation parameters remain the same for both design approaches, whereas for Creo further export options are unlocked in the assembly mode: Tessellation with parameters proportional to step size or nominal surface deviation (“pStep” and “pNdev”) can be chosen and the value range of the tessellation parameters expanded. It is worth mentioning that the models of the Creo software show no differences between the two export variants, proportional to step size and proportional to normal deviation, this is why only the result of “Creo-A-pStep” is included in the plots. For the tessellation of the assembly-based 3D model in Creo, the maximum value for each parameter that contributes to a higher tessellation accuracy is selected.

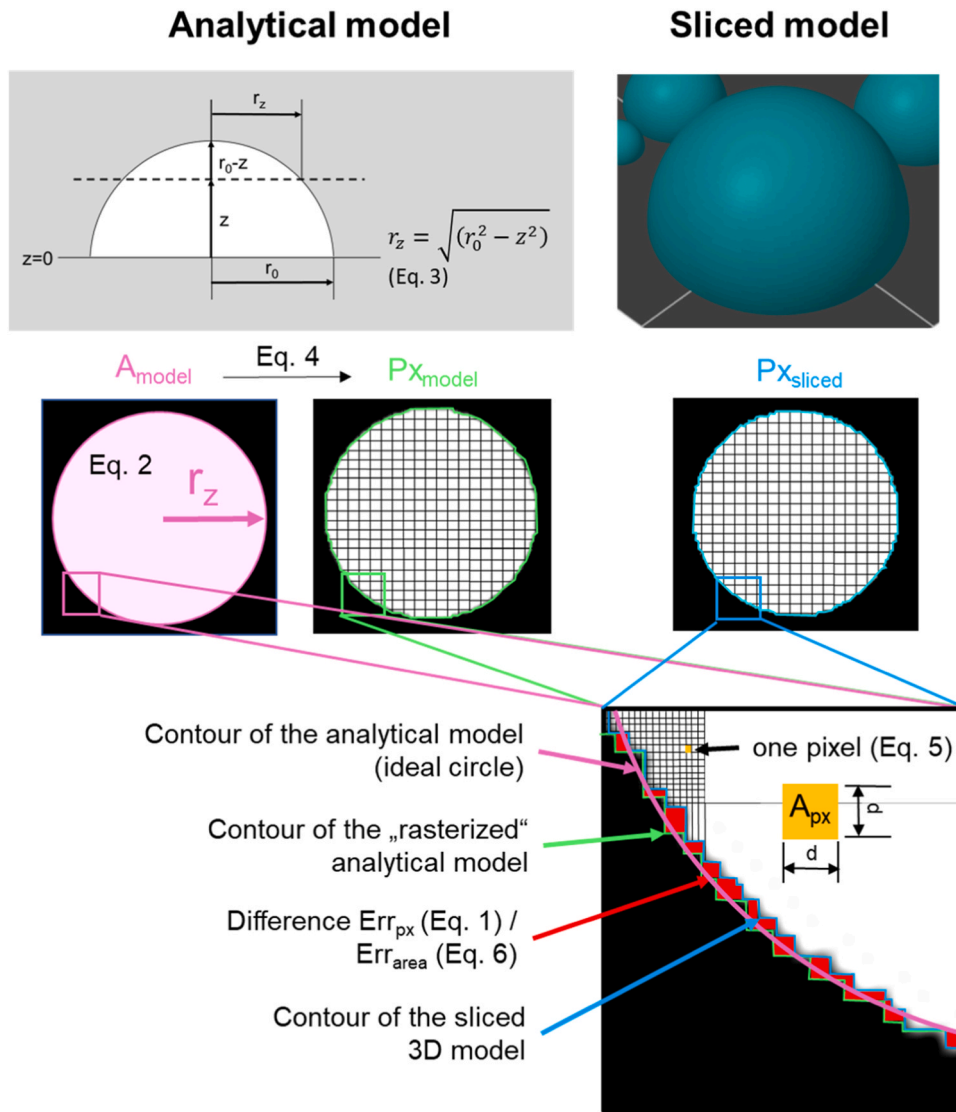


Fig. 3. Schematic visualization of the approach to define the difference between the cross-section area of the analytical model and the sliced model.

Table 1

Export settings of the CAD systems for the tessellation of the 3D models.

CAD software	Default Settings
Inventor Professional 2023	High resolution: Surface deviation 0.005 %, normal deviation 10°, maximum edge length 100 %, aspect ratio 21.5
Solidworks 2022	High resolution: Surface deviation 0.01238074 mm, angular deviation 10°
Creo Parametric 4.0	Part-based design: Surface deviation: 0.0003 mm, angle control: 0.1, step size: 0.01 Assembly-based design: Surface deviation: 0.01 mm, angle control: 0.5, step size: 0.1

### 3.4. Slicing

Three different open-access slicers are employed in this study, namely PRUSASlicer (Version 2.6.0-alpha3), 3DSlicer (Version 4.11.20210226) and a slicer based on python libraries, named “Slicer2” in this study. The resolutions applied in this study are 3600 dpi and 1800 dpi, equivalent to a pixel size of 7.05 μm and 14.1 μm, respectively. These values are similar to the typical dimensions of the printed droplets in MJ. The investigations for 3DSlicer and Slicer2 are all carried out with a nominal slice interval of 100 μm as for both slicers a lower slice

interval provokes the slicer software to crash.

The PRUSASlicer is an open-source software for both Material Extrusion printing (output: g-code) and LCD-based Vat Photopolymerization printing (output: stack of PNG images). Since both VP and MJ are based on binary images, this slicer is selected to be used for the creation of print images for MJ.

Table 2 shows the settings deployed in the PRUSASlicer. The size of the display and the number of pixels in this area define the resolution of the display. Elephant foot compensation is used in VP to ensure the first

Table 2

Settings of the PRUSASlicer 2.6.0.

Parameter	Value
Max print height	120 mm
Display width x height	25.4 mm × 25.4 mm
Number of pixels in x- and y-direction	3600 (x) and 1800 (y) pixels per inch
Printer scaling correction	x:1 y:1 z:1
Printer absolute correction	0
Elephant foot compensation and minimum width	0 mm
Printer gamma correction	0
SLA output precision	0.001 mm

couple of layers adhering well to the build platform by exposing them to a higher curing dosage and therefore favoring oversize. For MJ, no elephant foot compensation is needed. A printer gamma correction of 0 avoids blending of the boundary of the sliced object which would result in a grayscale image that is not processable by the MJ printer used in this study. The parameter “SLA output precision” does not have any effect on the outcome, thus the value is set to 1  $\mu\text{m}$ . PRUSASlicer is the only slicer software among the investigated ones that supports various 3D model formats such as AMF, 3MF, OBJ, and STP.

3DSlicer is an open source software intended for the use for medical 3D imaging based on medical images gathered from CT or MRT scans. The slicer software has been modified in-house and the imported 3D model is converted into a stack of TIFF images. In 3DSlicer the layer height is indirectly defined through the number of slices. To enable comparability of the output, the number of layers is chosen according to the number of sliced images generated by the PRUSASlicer (a slice interval of 100  $\mu\text{m}$  generated 63 layers, the first one being blank).

Slicer2 deploys the python libraries NumPy [53], PIL [54] and cv2 by OpenCV [55] to generate print images according to the following steps: (1) Importing the STL model; (2) Slicing the model in equidistant steps; (3) Creating contours of the intersected model; (4) Filling the contour with white pixels and (5) rendering of the slices in a given resolution and saving images as TIFF files (Tagged Image File Format). Slicer2 allows the specification of both the height and number of layers with which the slicing is conducted. For example, to generate 63 layers for a model height of 6350  $\mu\text{m}$ , a layer height of 100.79  $\mu\text{m}$  is required. Both 3DSlicer and Slicer2 supports STL model only.

### 3.5. Printing and experimental validation

An overview of the workflow for the experimental validation is given in Fig. 4. Firstly, the model is designed in a CAD software, which is then exported to an interoperable (tessellated) 3D model. This model is imported into a slicer software to be converted into layers of binary images representing the cross-sections of the imported 3D model along the slicing direction with increments as per the given layer height or the number of slices. The image files are saved as the raster image format TIFF so that they can be processed by the Material Jetting printer. Apart from the images, a job file specifying the printing settings, e.g., curing parameter, chuck velocity, z-axis increment, etc., is required by the printer to execute a print job.

To validate whether the detected improvement of the accuracy on the print data level is also evident in the printed specimen, element 1 of test specimen B is printed at various conditions and its surface profile recorded by the Keyence digital microscope VHX-7000. The specimen is printed at the 3D inkjet printer n.jet3D provided by Notion Systems, Germany, equipped with a Konica Minolta printhead KM1024iLHE-30 (nominal droplet volume 30 pl) containing 1024 nozzles and a native resolution of 360 dpi. KM1024iLHE is a piezo-based printhead that allows printing in binary and grayscale mode. For this particular printer setup, the waveform is fixed for each printhead during the printing process and only binary images can be processed, meaning that the nominal drop volume ejected by each nozzle is consistent. The average droplet volume is 26.48 pl. The print temperature of the transparent acrylate-based UV-curable ink is 35°C (viscosity 7.5 mPas, surface tension 35.6 mN/m at surface age 15 ms). The distance between the printhead and the substrate (equivalent to the curing distance) is

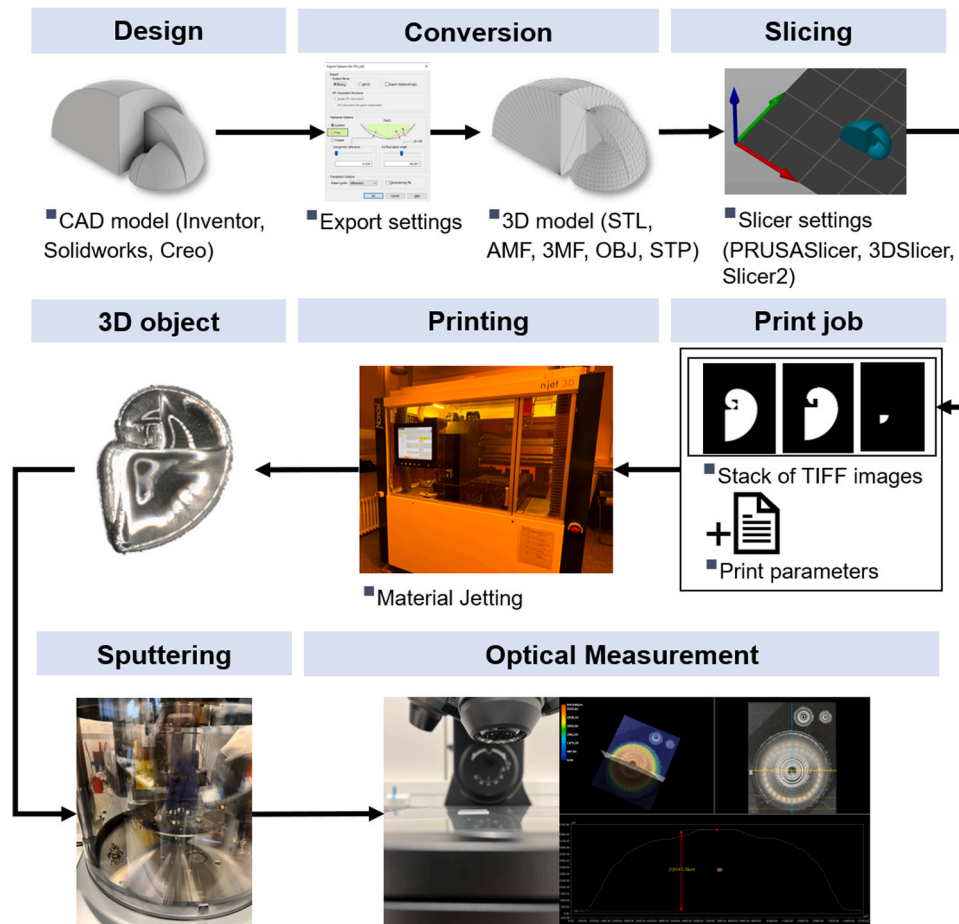


Fig. 4. Workflow of the experimental validation.

800  $\mu\text{m}$ . A 100  $\mu\text{m}$  thick PET foil is used as a substrate. Each specimen is printed 5 times within 6 hours to ensure statistical significance of the result and to minimize the variability induced by the variation of the ambient condition. The nominal resolution applied for the printing process is 1800 dpi and the resulting average layer height is 158  $\mu\text{m}$ . The curing is performed by the UV-LED lamp Phoseon FireEdge FE400 (emission window 10 mm) at an intensity of 8  $\text{W}/\text{cm}^2$  and at 365 nm wavelength for every layer immediately after printing. Both the printing and curing take place at a chuck velocity of 400 mm/s. Under these curing conditions, the printed object is exposed to UV radiation for 25 ms. Given the transparency of the printing material, the specimen's surface profile is sputtered with 10 nm chromium prior to the characterization step to enhance its visibility under the microscope. The sputtering is conducted with the device Q300T ES plus by Quorum, applying a sputter current of 120 mA for 60 s, in an argon-flooded environment.

## 4. Results and discussion

### 4.1. Conversion to tessellated format

#### 4.1.1. Influence of CAD software

To assess the performance of the three CAD software packages Inventor, Solidworks and Creo in terms of geometrical and dimensional deviation between CAD model and generated print data, various specimens have been exported and sliced on the PRUSASlicer.

Foremost, Fig. 5 shall elaborate how the following plots are to be interpreted and correlated to the 3D model. Each peak corresponds to the edge of a triangular facet which coincides with the surface of the original CAD model (points "L" and "M"), whereas each valley represents the deviation calculated for a sliced layer at a z-height which is located in between two vertices (points "l" and "m"). The characteristics amplitude, periodicity, number of peaks and the coefficients of the linear fit (intercept and slope) are determined and utilized to analyze the deviation curves of the assessed sliced images.

The amplitude describes the areal deviation resulting from the horizontal chord deviation at various z-heights. A z-height of zero refers to the base of the 3D model interfacing the slicer platform (point "A"). The periodicity, that is the distance between two adjacent peaks, corresponds to the vertical distance between two vertices of the triangular facets. The higher the z-value (slicing height), the closer the slice plane approaches the tip of the element (point "Z"). The number of peaks is

directly linked to the number of triangle facets. The slope of a linear fit of the curve quantifies the change of dimensional deviation along the model height. A value close to zero means that the deviation does not change when slicing at different z-positions. A consistent slope for all elements of the same model quantifies that all elements display the same magnitude of deviation, despite varying sizes. The intercept can be regarded as an approximation of the mean deviation of the base layer since the fitting curve lies between the peaks (vertices of the triangle facets) and local minima (horizontal chord distance).

The curves in Fig. 6 illustrate the dimensional deviation of the STL models exported from three different CAD software programs. The models are sliced on the PRUSASlicer. The entries in the legend indicate the nominal diameter of the elements and the title states the CAD software deployed. It is to be noted that in order to ensure visibility of all curves, the y-axis range of the Creo model (Fig. 6c) is set to  $\pm 50 \text{ mm}^2$ , while the curves of Solidworks ("SW", Fig. 6b) and Inventor ("Inv", Fig. 6a) are within a smaller range. An extract of the plots up to a z-height of 600  $\mu\text{m}$  with identical y-axis scaling is given in a red frame in addition to the original plots.

Although the three exported 3D models originate from the same design, the obtained deviation differs considerably depending on the CAD software that has been used for the export of the STL model. The plots in Fig. 7 depict the analyzed parameters for all elements in the 3D model which provides a more detailed picture of the discrepancies. It is noted that for all plots of this type the line connecting the data points is only added for the sake of better readability, but should not be considered for interpolating values between the data points.

Fig. 7a delivers the number of peaks counted for each element (10 in total) and the corresponding base diameters are displayed in the x-axis. In all three models the number of peaks drops the smaller the element becomes (the base diameter is double the model height). The number of peaks differs across the models, with the Inventor STL model (Inv) possessing the highest number of peaks for the largest three models. For elements of diameter 2.54 mm and smaller, the Solidworks STL model (SW) exhibits more peaks. The Creo STL model (Creo) contains the least number of peaks (approximately half of the peaks counted for the Inventor model) for all elements.

Fig. 7b depicts the coefficients of the linear fit of the deviations for each element. Each element displays a different slope (red data points) and intercept (blue data points). The intercept value decreases with smaller size of the elements, with the Creo model showing the most pronounced reduction of intercept value. The intercept values of the

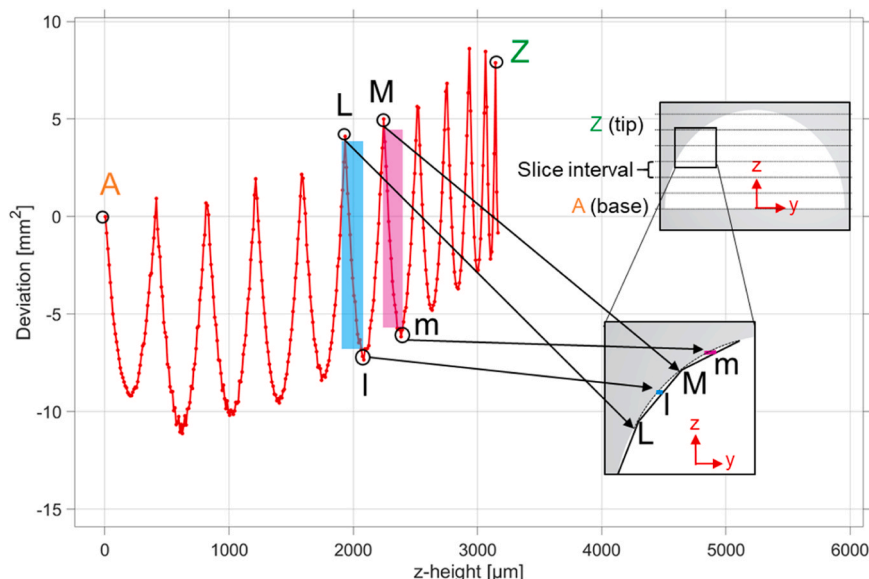


Fig. 5. Correlation between the obtained deviation curve and the tessellated 3D model.

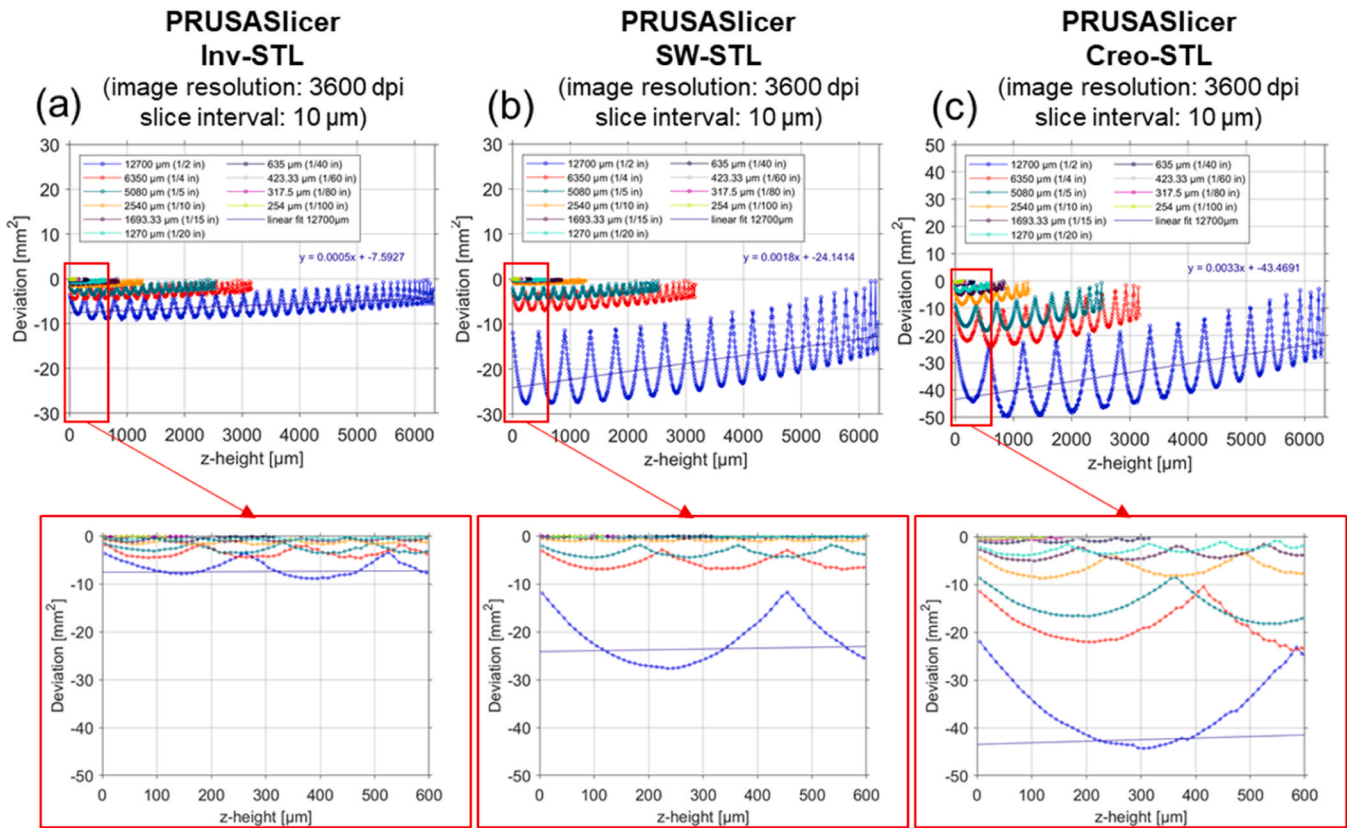


Fig. 6. Area deviation of the STL model test specimen B exported from the three different CAD software systems Inventor (a), Solidworks (b) and Creo (c) sliced on the PRUSASlicer.

Inventor model and Solidworks models are almost identical for elements with diameters less than 2.54 mm, but for larger elements, the intercept of the Inventor model decreases. For example, for the largest element with 12.7 mm diameter, the mean deviation of the bottom layers (intercept) of the Solidworks model is identified to be almost four times higher than the Inventor model ( $-24 \text{ mm}^2$  (SW) vs  $-7 \text{ mm}^2$  (Inv)). The dimensional deviation of the Creo model is even higher ( $-43 \text{ mm}^2$ ). All intercept values are negative.

Conversely, the slope values are all positive. While the slope of the Inventor model remains rather steadily at  $0.0005 \text{ mm}^2/\mu\text{m}$  (except for the very small elements), the slope of the Solidworks model becomes even less than the Inventor model for elements with base diameters smaller than 2.54 mm.

A similar behavior has been noticed for the periodicity as well (Fig. 7c). The periodicity value of the Creo model stays well below the other two models. In general, the standard deviation is relatively large for every element which could be linked to the characteristics of the curve that the distance between two peaks reduces the closer the slice plane approaches the tip of the hemisphere (Fig. 6).

From the plot shown in Fig. 7d, it can be inferred that the amplitudes of all three models diverge in particular for larger elements. The average amplitude for the largest element is reported to be  $\pm 27 \text{ mm}^2$  for the Creo model,  $\pm 17 \text{ mm}^2$  for the Solidworks, and  $\pm 6 \text{ mm}^2$  for the Inventor model.

In all plots, the amplitude diminishes the smaller the element becomes because of the shifting of the troughs closer to the peaks, while the peaks remain at the same absolute value. This behavior is illustrated in Fig. 8, which shows the same results as in Fig. 6, but arranged according to the nominal radius of the sliced image. From this plot, it is evident that for all investigated CAD software, the target accuracy applied during the tessellation process of the STL model is governed by the element's size, and not by the total size of the imported 3D model.

The periodicity values of all plots are subject to very large standard deviation due to the fact that the distances between two adjacent peaks shorten the closer the assessed layer is located to the tip of the hemispherical element. The tessellation facets become more inclined towards the tip in order to fit into the curved shape of the hemisphere. Subsequently, the increased inclination angle reduces the "vertical height" (z-direction) of the facet and as a result, the distance between two vertices of two adjacent triangular facets shortens (Fig. 9).

The negative intercept values observed for all models suggest an undersize of the base layers of the assessed models. The undersize is due to the tessellation approach, where the vertices of the triangle facets are positioned along the 3D model surface, necessitating the edges connecting two vertices to pass beneath the model's surface (Fig. 9). The undersize of the sliced models has also been noticed by Pinto et al. [20].

The negative intercept values reduce and approaches the zero level with decreasing diameter. This is expected, as the deviation only occurs at the contour of the sliced model. A smaller model (element with smaller diameter and thus smaller perimeter) generates less deviation compared to a large model. The mathematician Gauss proposed that the lattice points/number of square cells confined by a circle is approximately the surface area with an error which does not exceed the circumference [56]. This explanation is equally applicable to the observation that the (negative) deviation minimizes when the layer is approaching the tip of the hemisphere (indicated by a positive slope) where the cross-sectional area is becoming smaller as well.

Furthermore, a correlation between the working principles of the CAD software, the size of the elements featured in the 3D model and the dimensional deviation has been identified. The CAD software Inventor creates models with higher accuracy (perceived by lower amplitude, periodicity and more peaks) in particular for elements with diameter greater than 2.54 mm, while for smaller features the models of the CAD software Solidwork are more superior in terms of accuracy.

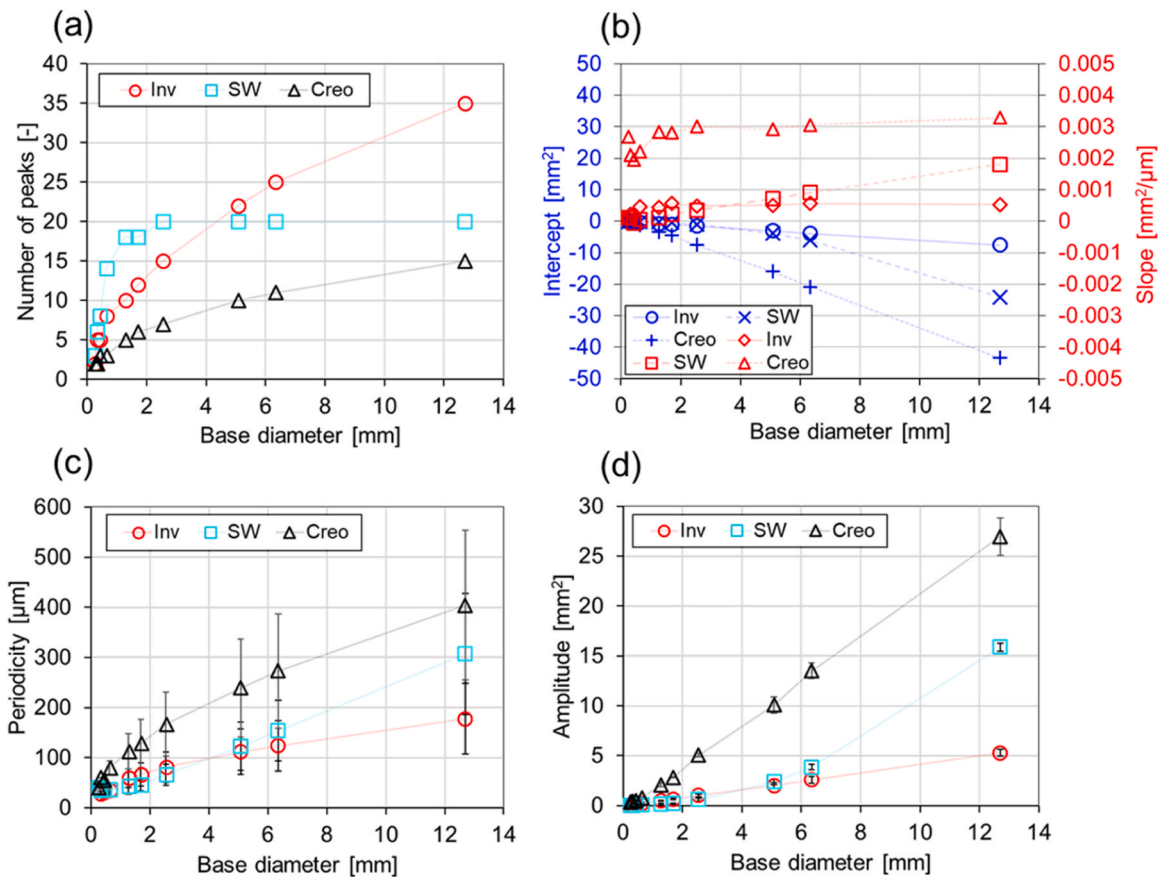


Fig. 7. Number of peaks (local maxima) (a), linear fit coefficients intercept (b, blue) and slope (b, red), periodicity (c), and amplitudes (d) of the deviation curves of all elements shown in Fig. 6.

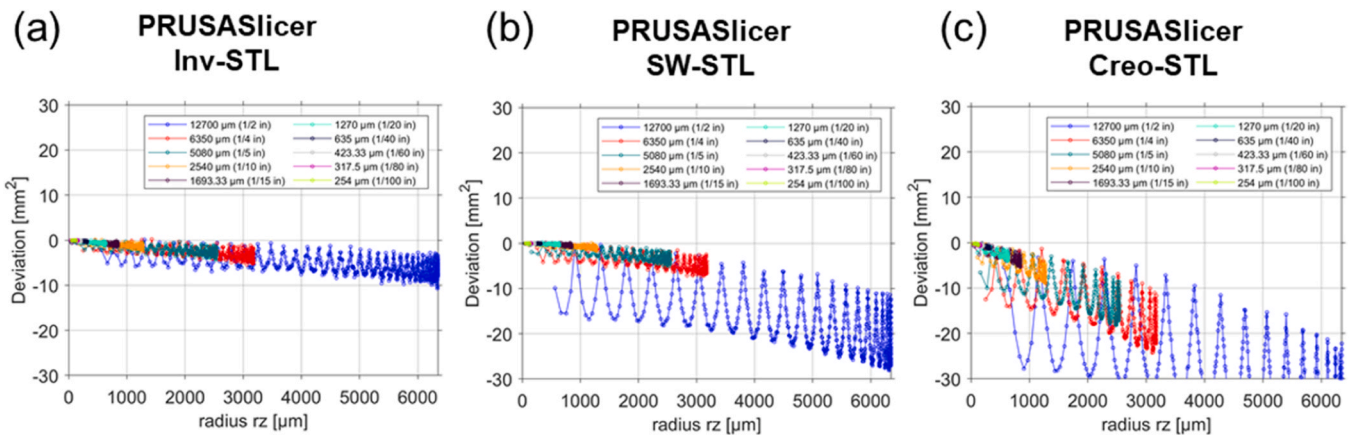


Fig. 8. Area deviation as shown in Fig. 6 arranged according to the corresponding nominal radii  $r_z$  of the sliced elements of test specimens B at various z-heights.

This distinct behavior proposes that in the software Solidworks, the targeted accuracy during the tessellation procedure applied by the software algorithm is calculated relatively to the size of the element. Hence, the larger the element becomes, the greater the targeted absolute dimensional deviation and the larger the triangular facets are, that are utilized for the tessellation. The software Inventor, on the contrary, keeps the absolute targeted dimensional deviation in check throughout all elements, evident in the continuously rising number of peaks with larger elements. It has to be noted, that above the diameter 2.54 mm the disparity between these two CAD software packages becomes very distinct. The dimensional deviation reported for the largest element of

the Solidworks model is four times greater than the one in the Inventor model. Meanwhile, the analysis of the Creo model reveals that the dimensional accuracy is by far the lowest among the investigated models, indicated by a higher intercept and slope values as well as by greater amplitudes and periodicities. The considerably higher deviation reported for the software Creo compared to other CAD systems has also been observed by Hällgren et al. [33].

The different operating principles of CAD software affect the change of deviation along the element's height as well. The slope of the Solidworks model experiences a consistent decrease of the value starting from a deviation of approx.  $0.0018 \text{ mm}^2/\mu\text{m}$  for the largest element, which

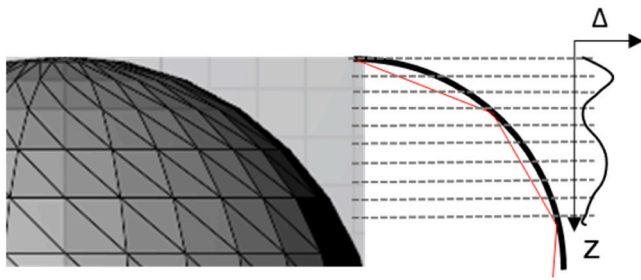


Fig. 9. Tesselated model and the chord deviation  $\Delta$  along the slice direction  $z$  (model's height).

reaches  $0.0001 \text{ mm}^2/\mu\text{m}$  for the smallest element. The greater slope values imply a more distinctive reduction of the dimensional deviation when assessing layers closer to the tip of the hemisphere. Conversely, the more accurate Inventor STL model exhibits a slope that is relatively consistent, the values ranging close to the zero level (from  $0.0001$  to  $0.0005 \text{ mm}^2/\mu\text{m}$ ). It can be concluded that the degree of the change of the dimensional deviation along the element's height is correlated to the overall deviation of the element. For small elements, it is their perimeters which define the resulting dimensional deviation caused by the rasterization process, whereas for elements with larger sizes, the obtained dimensional deviations depend mainly on the tesselation process. Consequently, even though the Creo 3D model is inferior in terms of overall accuracy compared to the models of the other two CAD software packages, this behavior does not apply to elements smaller than  $635 \mu\text{m}$  in diameter. In this size range, the dimensional accuracy of the Creo model is on par with the other two 3D models.

4.1.2. Design as part-based vs assembly-based CAD model

Fig. 10 shows the characteristics of the obtained deviation results of the three CAD models that are designed and saved as an assembly STL model, indicated by the attribute “-A” (“-P” stands for part-based model).

The Inventor assembly-based model exhibits less dimensional deviation over the part-based model, with the level of reduction depending on the size of the element, although mainly contributed by the substantial improvement of accuracy for very small elements. Starting from a diameter of  $2.54 \text{ mm}$ , the resolution of tesselation diminishes the larger the elements become. This change is quantified by the slight reduction of the intercept (Inv-A, Fig. 10b, blue), especially for larger elements, and a reduced slope value in particular for small and middle-size specimens (Inv-A, Fig. 10b, red). With regards to the largest element, the intercept decreases from  $-7.59 \text{ mm}^2$  (Inv-P) to  $-5.36 \text{ mm}^2$  (Inv-A), equivalent to a reduction of the dimensional deviation by 29 %.

The slope is reduced from  $0.0005 \text{ mm}^2/\mu\text{m}$  (Inv-P) to  $0.0003 \text{ mm}^2/\mu\text{m}$  (Inv-A). A higher number of peaks has been identified for the Inventor STL assembly model.

In contrast, the assembly-based STL model exported from Solidworks (SW-A) shows no difference compared to the corresponding part-based STL model, which is also evident by the unchanged file size and characterized by the identical number of peaks (Fig. 10a) and coefficients of the linear fit (Fig. 10b).

The Creo assembly model (Creo-A) achieves the most substantial improvement of the accuracy in relation to the part-based design among the three investigated 3D models. For the assembly model, the intercept (Fig. 10b, blue) of element 1 changes from  $-43.5 \text{ mm}^2$  to  $-0.8 \text{ mm}^2$ , while the slope value (Fig. 10b, red) decreases to almost zero from  $0.0033 \text{ mm}^2/\mu\text{m}$ . The number of peaks (Fig. 10a) increases from 17 peaks to more than 190 peaks.

The flattened curve of the Inv-A model for elements greater than  $2.54 \text{ mm}$  diameter points to the fact, that the maximum acceptable deviation of the Inventor part-based model (Inv-P) is lower than the assembly model. This means that despite the increasing size of the elements, Inventor's assembly model keeps a constant number of facets as long as the resulting increase of surface deviation remains below the maximum (allowable) deviation. This behavior is similar to the results obtained for the Solidworks part-based model (SW-P), which shows a saturation of the number of peaks for larger elements as well.

The significant improvement of the dimensional deviation for smaller elements up to a diameter of  $2.54 \text{ mm}$ , which is evident for the Inventor assembly model Inv-A and both Solidworks models (SW-P, SW-A), suggests that the tesselation process operated with a factor for lowering the acceptable deviation for elements with smaller radii, necessitating the CAD software to increase the number of facets strongly for very small elements. Without this factor, a smaller element would be tesselated with just few triangles, as the tesselation error would still be within the acceptable scope. This accuracy-improving factor might be defined by two values – the size of the element and a threshold when this factor comes into play. The threshold could be correlated to the size of the model, as the three 3D models Inv-A, SW-P and SW-A, for which it is assumed that this corrective factor has been deployed, share the same behavior: Between the elements 4 (radius  $1.27 \text{ mm}$ ) and 3 (radius  $2.54 \text{ mm}$ ), the steady increase of peaks terminated. Given that the size of the investigated test specimen B is  $17.85 \text{ mm}$  (x) x  $19.12 \text{ mm}$  (y) x  $6.35 \text{ mm}$  (z), the threshold could be determined as  $1/10$  of the x or y dimension. For instance, for Creo it is reported that the maximum chord height is multiplied by a factor termed control angle (value range 0–1) when the radii of the element is smaller than  $1/10$  of the part size to ensure small elements to be tesselated more accurately [57].

It is to be noted, that the reduction of the deviation comes with a price, that is the increase of file size. The file size of the more accurate

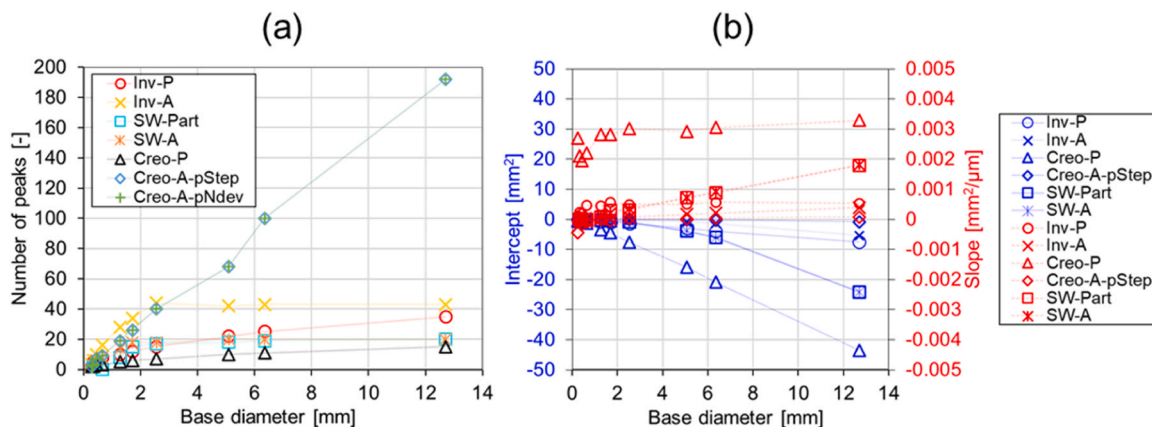


Fig. 10. Number of peaks (a) and linear fit coefficients intercept (b, blue) and slope (b, red) of the deviation curves of all elements of test specimen B designed as part-based (-P) and assembly-based (-A) CAD model.

assembly model of Inventor is almost six times greater than the part-based model (Fig. 12).

The largest improvement of the dimensional accuracy could be observed for the Creo CAD software, because the assembly mode in Creo allows further settings to be specified, such as proportional slicing according to the step height or nominal deviation. Activating either of these options and applying the most accurate tessellation settings allowed by the software, a 3D model could be exported that achieves a reduction of the dimensional deviation by 98 % over the part-based model. Yet, this advancement comes with a considerably increase in file size. The option to create facets proportional to the step size (“prop step”) resulted in the largest file size among all other models examined in this study (Fig. 12).

4.1.3. Deploying different 3D model formats

Fig. 11 visualizes the characteristics of the deviation curves obtained from slicing models of various data formats, namely STL, OBJ, 3MF, AMF and STP, on the PRUSASlicer.

The plots in Fig. 11 a,c,d, disclose that the 3D models exported to the formats STL (“Inv-STL”) and OBJ (“Inv-OBJ”) are identical, whilst the object imported as STP model (“Inv-STP”) denotes greater slopes and more negative intercepts (Fig. 11a), less number of peaks (Fig. 11c), and larger amplitudes (Fig. 11d). For example, the intercept value of the largest element of the STP model is  $-11.9 \text{ mm}^2$ , approximately 1.5 times higher than the value of the STL/OBJ model ( $-7.64 \text{ mm}^2$ ) exported from Inventor.

Similarly, the 3MF, AMF and STL models exported in Solidworks (“SW-3MF” and “SW-AMF”) are essentially the same, apparent in the

unchanged deviation curves for all elements and the consistent number of peaks (Fig. 11b, c). The mean amplitudes of the 3MF model are slightly less than the other two formats, but taking the large standard deviation into consideration, the changes can be considered negligible (Fig. 11d).

The results are all derived from PRUSASlicer, as among the investigated open-source slicers, only this slicer software is capable of importing various formats of 3D models, namely STP (not tessellated format), 3MF, AMF and OBJ.

With regards to the non-tessellated STP model, the PRUSASlicer seems not to slice the 3D model directly, but tessellates it upon import. The tessellated STP model created by the PRUSASlicer is less accurate compared to the “high-quality” tessellated model obtained from the Inventor software.

Moreover, the deviation curves observed for the formats STL, OBJ, 3MF and AMF are all overlapping. This implies that utilizing different formats does not change the geometry and accuracy of the tessellated model, but only affects how the descriptive information of the triangle facets is stored in the file. This result contradicts with the advantages reported for the 3D model format AMF, which is capable of representing a curved surface by utilizing curved triangular facets. A closer look into the exported ASCII-encoded AMF file in a text editor confirms that the model’s surface is still approximated by planar triangle facets, which explains the lack of difference to the corresponding STL model. However, the CAD software Creo does exploit the advantage of the AMF model by employing curved triangular facets in the exported AMF 3D model, indicated by the <edge> elements in the AMF file. However, upon import of this file, the PRUSASlicer prompted an error as these

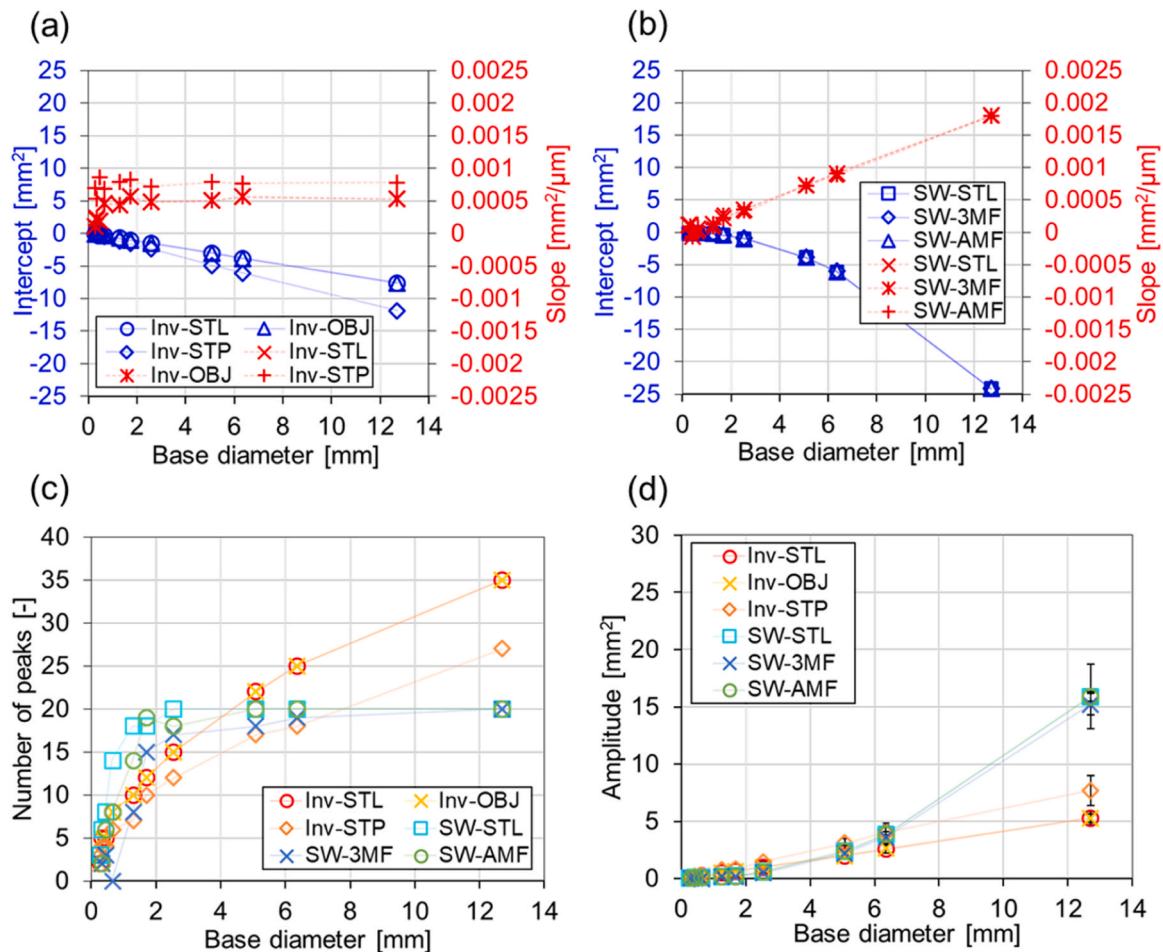


Fig. 11. Linear fit coefficients intercept (a, blue) and slope (a, red) of the deviation curves of all elements in test specimens B exported as different 3D model formats in Inventor (a), in Solidworks (b), and their corresponding number of peaks (c) and amplitudes (d).

<edge> elements could not be processed by the slicer software. In order to leverage the benefits of this promising AMF data format, the collaboration of both CAD and slicer software developer is central.

Overall, the edge of deploying different 3D model is the reduction of file size. 3MF offers the leanest file size even in an uncompressed stage (Fig. 12). For Solidworks, the AMF model takes up less memory compared to the STL model, whereas for Creo it is the opposite case – this contrasting behavior can be explained by the additional <edge> elements in the Creo AMF model which add to the file size. Saving the STL model encoded as a binary file reduces the file size by about 5 times compared to an ASCII-based file.

#### 4.2. Slicer-induced deviations

The investigation of the slicer-induced deviation in this Section is divided into two parts. Firstly, the performance stability of the three deployed slicers is scrutinized by assessing the dimensional deviation of the cylinder-based test specimen A (Fig. 13). This result is compared to the results of test specimen B (hemisphere-based) in Fig. 14 to assess if the slicers treat objects with curvature in all three dimensions differently (the base diameter size and the positions of the elements are the same for both test specimens).

As a general observation, the mean deviation of the cylindrical elements increases, the larger the examined element is (Fig. 14). The deviations assessed for 3DSlicer and PRUSASlicer are all ranging in the negative region, while the sliced images of Slicer2 exhibit a positive deviation, implying an oversize. The mean deviation of the 3DSlicer remains greater than PRUSASlicer throughout all elements, but especially for the larger elements, the difference becomes more distinct. For example, the mean dimensional deviation of 3DSlicer for the cylinder with diameter 12.7 mm is almost 10 times higher than that of the PRUSASlicer (Fig. 14).

Generally, the least deviation for all cylinders has been reported with the PRUSASlicer (-3.19 mm<sup>2</sup> (2.5 %, largest cylinder) to -0.07 mm<sup>2</sup> (smallest cylinder)). Slijovic et al. (2019) also reported a similar range of deviation of 1.34–6.72 % for material extrusion 3D parts sliced with Slic3r, the slicer on which PRUSA is based on [58]. 3DSlicer, in contrast, produces dimensional discrepancies between -37.49 mm<sup>2</sup> (29 %, largest cylinder) and -0.07 mm<sup>2</sup>. Slicer2's performance lies between these two slicers.

In addition, the manner in which the deviations vary along the model's height differs among the investigated slicer software. In the case of PRUSASlicer, the dimensional deviations of the smaller elements are consistent which is to be expected, as the diameter of the cylinder does not change along the slice direction. However, the largest element shows a deviation pivoting between -4.0 mm<sup>2</sup> (-3.2 %) and -2.4 mm<sup>2</sup> (-1.9 %) (Fig. 13a). The largest deviation (local minimum) is reached every 3100  $\mu\text{m}$  in z-direction (slice direction) and the lowest deviation is obtained half-way (around 1500  $\mu\text{m}$  or 4800  $\mu\text{m}$ ).

The curves plotted for 3DSlicer are showing variations as well,

although the deviation curve acquired from the largest element alternates between a curved and a constant section, the width of each section spanning a z-range of 2160  $\mu\text{m}$  (Fig. 13b). The deviation of the largest element pivots between -38.1 mm<sup>2</sup> (-30 %) and -36.5 mm<sup>2</sup> (-29 %). The wave-like deviation curve of element 3 (diameter 5080  $\mu\text{m}$ ), on the other hand, resembles the curve identified for the largest element sliced with PRUSASlicer. The deviation stays within the boundaries of -1.81 mm<sup>2</sup> (-9 %) to -1.47 mm<sup>2</sup> (-7 %) and the local minimum is located at a z-distance of 1260  $\mu\text{m}$  (base layer is equivalent to a z-height of 0 mm).

For unknown reason, Slicer2 failed in slicing element 2 (diameter 6350  $\mu\text{m}$ ) and element 3 (diameter 5080  $\mu\text{m}$ ) correctly, both of them only appearing as a contoured pattern in the slice image, thus their results were excluded from this plot (Fig. 13c). Compared to the results of the other two slicer software, the deviation reported for each slice of the 3D model is subject to a higher and irregular variability with higher frequency along the model's height. This variability is expressed in a high standard deviation of up to 21 % of the mean value (Fig. 14). The values for the largest diameter (12.7 mm), for example, fluctuate between 9.47 mm<sup>2</sup> (7 %) and 14.78 mm<sup>2</sup> (12 %).

The results shown in Fig. 13 expose varying performance stability across the slicers. The instability along the slice height might be linked to the different workflows the slicers use to generate raster images from a tessellated 3D model. While PRUSASlicer most likely creates first a vector image which is then converted into a raster image, 3DSlicer divides the imported 3D model into elements according to a given resolution and saves the raster 2D image as TIFF file. Slicer2 generates contour lines by determining the intersection points of the triangle facet with the z-plane of interest which are then connected by a line drawing algorithm in a pixel-based manner. The area enclosed by the contour is filled and the image is saved as a raster TIFF-image. The underlying rasterization algorithm is unknown for all slicers, however it has been reported that some algorithms are more prone to instability, in particular those who deploy a division operation, which could explain these variations [59].

Furthermore, all three slicers seem to perform differently with regards to the areal deviation depending on the diameter of the sliced cylinder. Fig. 14a displays the relative deviation in relation to the perimeter and to the surface (only for the results of 3DSlicer). From this plot, it is evident that the deviations observed for all examined models are less than the perimeter, which aligns with the assumption proposed by Gauss that the error when approximating a circle by square elements stays less than the circumference [56].

However, for 3DSlicer, in particular, the relative deviation increases the larger the model becomes, whereas for PRUSASlicer and Slicer2 the deviation decreases. 3DSlicer, as explained above, most likely rasterizes the 3D model into cubic elements first, whereas the other two slicers create raster images after slicing the model into 2D cross-sectional images. This means, that during the 3D rasterization process by 3DSlicer, three-dimensional segments on the boundary of the imported model are most likely removed which introduces greater areal deviation compared to a rasterization step of a 2D image.

Only Slicer2 is exhibiting a positive areal deviation which means that the cross-sectional area of the sliced model is larger than the analytical model (ideal circle). Since both Slicer2 and PRUSASlicer are generating 2D slices in a relatively short amount of time, and can handle larger models as well, it is likely that both slicers deploy a similar approach of generating sliced images. They could utilize a line drawing algorithm, such as the Bresenham algorithm [60] or the digital differential analyzer algorithm [61] to draw the contour of the sliced model at different z-height. Bresenham algorithm allows defining an error term that decides the distance between the intersection point of the line with a pixel and the coordinates of the previous adjacent pixel that is acceptable to turn on the intersected pixel [62]. Slicer2 might deploy a line drawing algorithm with a particular decision term that generates contour lines that are drifting further away from the ideal shape. Another explanation

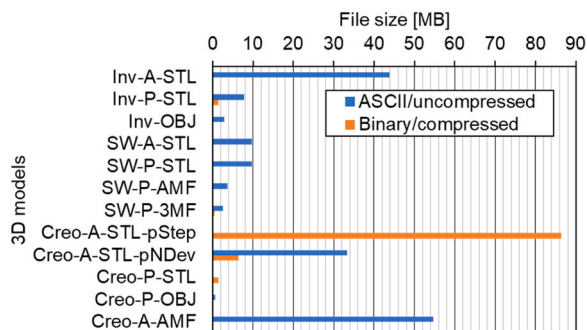


Fig. 12. Comparison of the file sizes of identical 3D models designed and exported under various conditions.

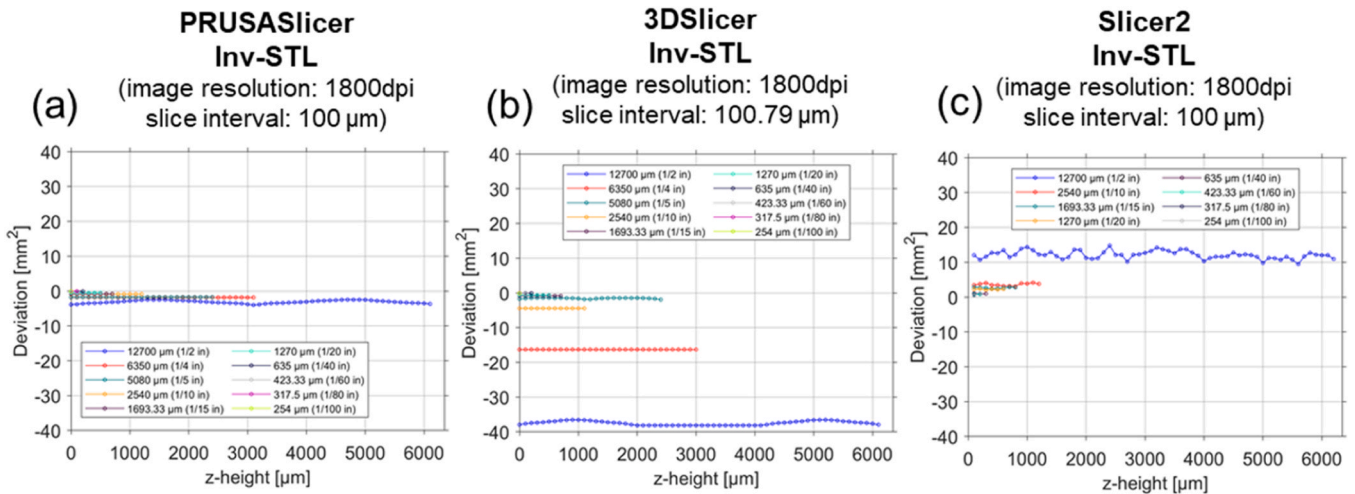


Fig. 13. Dimensional deviation of test specimen A (cylindric elements) along the z-height (build height) exported from Inventor as STL and sliced on the three different slicer software PRUSASlicer (a), 3DSlicer (b) and Slicer2 (c).

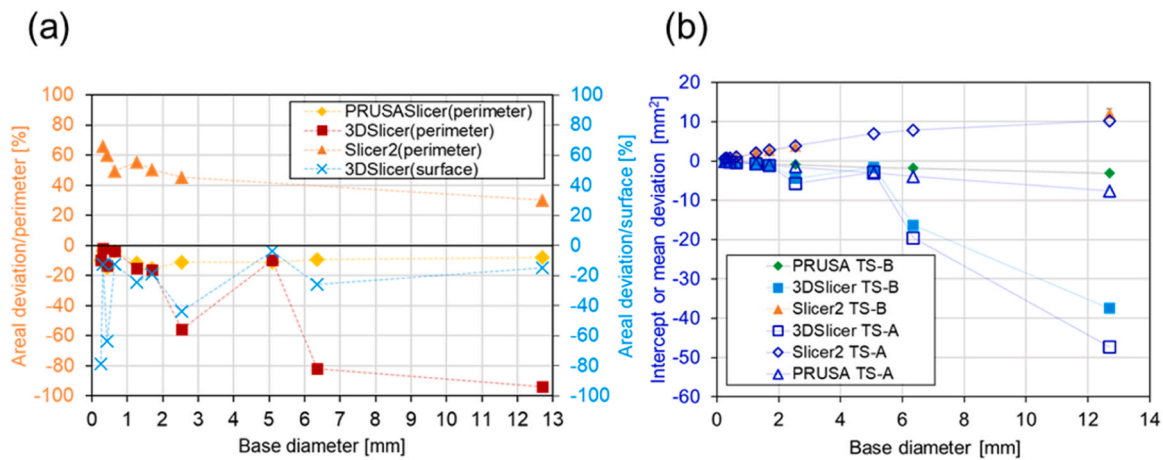


Fig. 14. Relative areal deviation of test specimen A with respect to the perimeter of the element (a) and intercept values (applicable only to test specimen B, TS-B) of the STL model exported from Inventor and sliced on the three slicer software 3DSlicer, Slicer2 and PRUSASlicer.

for the smaller cross-sectional area of the PRUSASlicer could be linked to the option of the slicer to apply anti-aliasing to the sliced model. Since the anti-aliasing has been deactivated in this study, pixels that would have appeared in a grayscale level are turned off, thus leading to a smaller area of the cross-section.

Fig. 14b plots the intercept values of the linear function fitting the dimensional deviation of the elements of test specimen A (cylinders, TS-A) and B (hemispheres, TS-B), exported from Inventor and sliced by the three different slicers, PRUSASlicer, 3DSlicer and Slicer2. As a general observation, the obtained deviations of the hemisphere-based test specimen B for all three slicers are shifted towards the zero level compared to the results of test specimen A. The negative deviation increases by 200 % for PRUSASlicer and by 18 % for 3DSlicer when slicing a hemisphere, whereas for Slicer2, the positive deviation is almost consistent, if taking into account the variance of the slicer.

The large disparity in dimensional deviation between slicing a cylinder and a hemisphere, despite their equal base diameter, could be due to an incorrect z-height of the reference layer based on which the dimensional deviation is calculated (Eqs. 2 and 4). The plane to which the slice image is compared is likely below the actual z-height from which the slice image is derived, meaning that the nominal circle radius  $r_z$  is larger and thus the already existing undersize induced by the slicer

itself is further enlarged. In order to understand the real cause and verify this hypothesis, the results of the experimental evaluation could shed light upon this matter.

### 4.3. Experimental validation

Several specimens were printed in order to validate whether the changes of the accuracy identified for the print data is evident in the printed specimens as well. Fig. 15 displays the obtained surface profiles of the printed specimens in print direction (Fig. 15a,c,e, attribute "PD") and parallel to the printhead axis (Fig. 15b,d,f, attribute "PH"), as well as the ideal shape of element 1, indicated as a red color line. The dashed lines mark the lower and upper bound accounting for the standard deviation of the measured data, displayed in the same color.

All printed samples are not perfectly hemispherical and are slightly taller than the reference ideal geometry (hemisphere). Each specimen exhibits at the base a much greater width (up to 8000 µm radius). This means that the base area of all printed specimens is oversized by around 1.5 mm in diameter which contradicts to the results obtained from the theoretical investigation. The theoretical results indicate that the under- and oversize of the sliced base layer should manifest as a radius de- and increase within the range of -1.09 mm and +0.31 mm in the printed

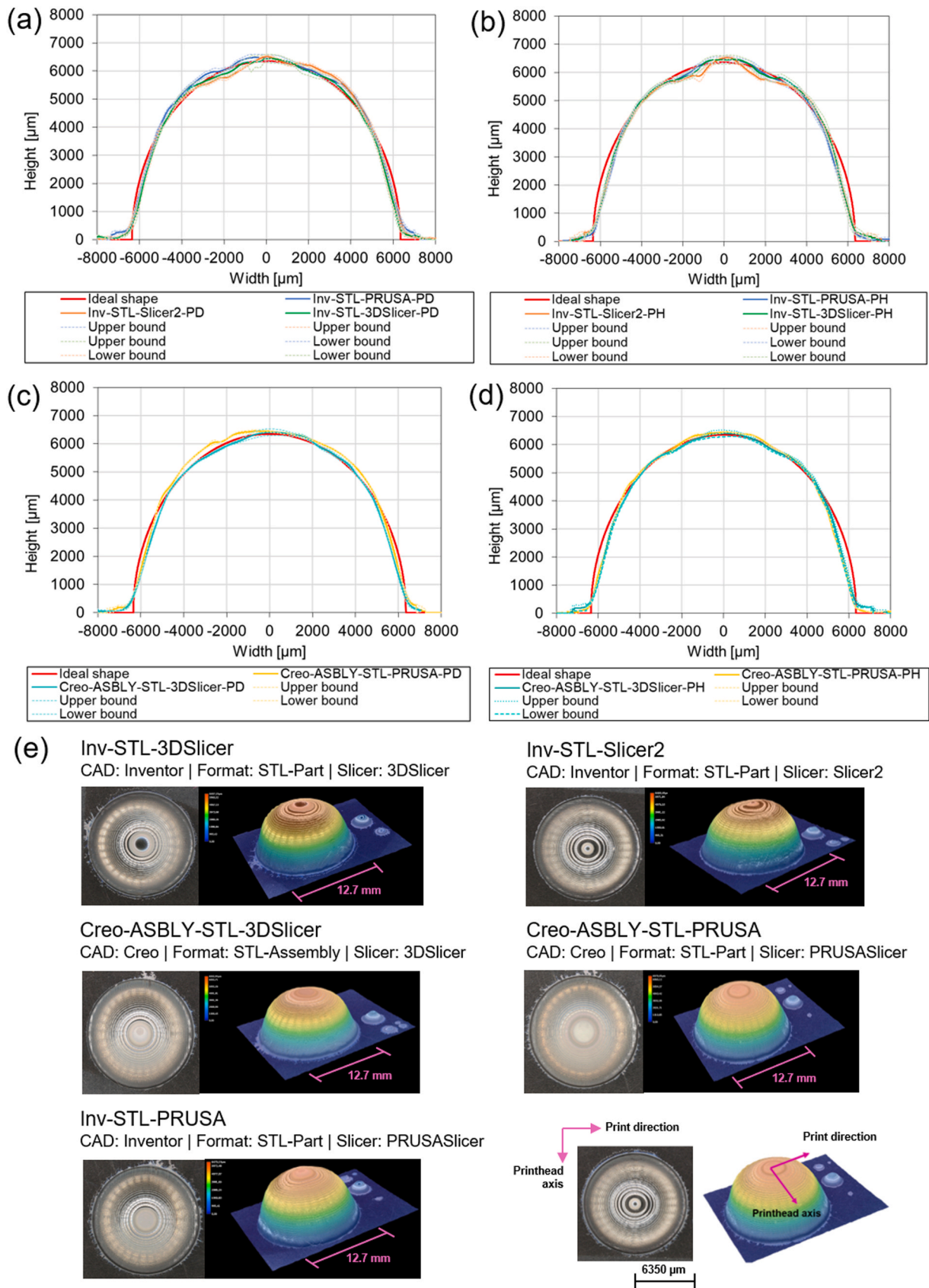


Fig. 15. Surface profile of the printed hemispheres (base diameter 12.7 mm) in print direction PD (a, c) and parallel to printhead axis PH (b, d) and printed specimens captured on the microscope (e).

specimen (Table 3). Considering that the measured oversize exceeds the print data-related deviation, the actual size of the base is most likely masked by other factors, such as by the surface wetting behavior between the first layer and the substrate [63].

After printing 2–3 layers, that is beginning from a height of approximately 500  $\mu\text{m}$  up to a z-height of roughly 4000  $\mu\text{m}$ , the printed specimen becomes narrower than the ideal shape. All three specimens are almost identically shaped in this lower half of the hemisphere. Above this height and up to a height level of about 5550  $\mu\text{m}$ , the shape becomes moderately broader than the ideal shape.

The irregular shape might be caused by the changing degree of how the layers overlap in the course of the printing process. Due to the increased curvature of the hemisphere towards the tip, the diameter difference between two subsequent layers increases, if maintaining the same slice thickness. In the case of small diameter difference between subsequent layers, the contour of the newly printed pattern is most likely printed onto the rim area of the former layer, which is typically slightly curved due to the hemispherical shape of the printed droplets (Fig. 16). This curved rim zone favors the flowing of the newly printed droplets towards the contour of the previous layer which smoothens the transition between the contours of two overlapping layers. However, if the diameter difference becomes larger as it is the case for the layers around the tip area, the contours of two following printed layers are distanced widely, resulting in less or no smoothening that is visible as so-called “stair-case” [64] or “stair-stepping” effect [65] (Fig. 16).

Furthermore, the profiles measured along the print direction starting from a z-height of 500  $\mu\text{m}$  are all wider (closer to the ideal shape) than the ones parallel to printhead axis. The different outcome of the printed part in dependence of the directions could be linked to the fact that the tolerances in both directions are governed by different factors. While the accuracy in print direction depends on the machine axis resolution, the accuracy parallel to printhead is controlled by the printhead’s manufacturing tolerance and the number of offsets necessary to achieve a higher print resolution than the native resolution of the printhead which could result in an accumulation of the printhead’s native tolerances.

Further up approaching the tip, the actual shape starts to narrow again and the degree at which the diameter decreases varies depending on the different data preparation conditions. The plots in Fig. 15a and b depict the surface profile of the same specimen exported by Inventor, sliced by three different slicers and printed with the same print settings. The most pronounced difference between these printed specimens can be found around the tip area of the element. The printed specimen sliced with “Slicer2” shows a pointier tip, while the specimens sliced with PRUSASlicer and 3DSlicer end up with a flatter tip, with the PRUSA samples being the flattest one among the three variants.

The difference between the Creo part-based model and the assembly-based model is depicted in the plots Fig. 15c and d. All specimens were sliced on the PRUSASlicer. The yellow curves in both plots show that the Creo assembly model presents the closest approximation to the ideal shape among the three printed specimens with regards to the upper half of the element. The part-based models (blue and black lines) are shaped similarly, both containing a sudden tapering at a height of around 5550  $\mu\text{m}$  which results in a pointier tip than the assembly-based specimen (yellow).

A closer look into the print data reveals that the cause of the variation of the tip shape must be induced by the slicing process. PRUSASlicer

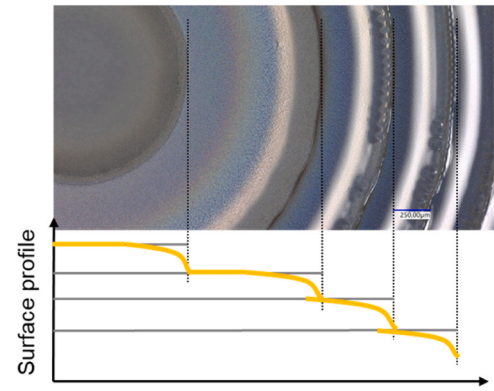


Fig. 16. Top view of a printed specimen (top 4 layers) and schematic representation of the surface profiles of each layer (yellow curve) (scale bar represents 250  $\mu\text{m}$ ).

might retrieve the first sliced image, representing the base layer from the model at a certain z-height distanced from the platform. Then, a section of unknown thickness might be cropped from the base of the model in reference to the platform (the height should range between 300  $\mu\text{m}$  and 350  $\mu\text{m}$  based on some pre-tests, but no precise specifications are provided by the developers of the slicer). For this reason, an offset of 300  $\mu\text{m}$  has been added to the 3D model during the design phase. The new model reduced by the cropped height will then be sliced with the given layer thickness starting from the new bottom plane (Fig. 17). The generated stack of sliced images consists of 41 layers, the first layer being blank (bottom layer) and the remaining 40 layers showing the cross-sections of the model along the z-direction. This unknown offset due to the cropping step might also explain the negative mean deviation of PRUSASlicer observed in the results depicted in the previous Section. If the base of the imported model is partly cropped, the sliced area of the hemisphere at a given z-height is in reality smaller in size than the nominal size as essentially a layer further up is assessed.

The slicer 3DSlicer generates a similar set of images resulting in a comparable tip shape in the printed specimen although no cropping has been performed beforehand. 3DSlicer references the coordinate system of the model, defined during the design in the CAD software, to the slicer platform’s coordinate system. Even though the 3D model has been designed in the CAD software on the x-y plane ( $z=0$ ), upon import in the slicer, the model has been shown in the log-file to be aligned to a z-point of  $-7.77611\text{e-}16$  mm. Despite the offset being very minor, the slightly shifted origin most likely caused the model to be partly ignored in the upper region (Fig. 17). Since the slicing of this slicer starts from the tip of the model, the 40th layer (base layer) is beyond the physical model, resulting in a blank layer for the bottom layer. Ideally, the slicer should ensure that the imported model is precisely aligned to the zero point of the model to avoid such kind of error.

Slicer2 generates 40 layers with a slice interval of 158  $\mu\text{m}$ . Since the model height is not an integral multiple of the layer height of 158  $\mu\text{m}$  and the slicing direction begins at the bottom and moves to the top, the last slice is located minimally below the tip which is printed as a circle with a very small diameter (Fig. 17). This last image accounts for the pointy tip visible for the printed object. Slicing with an exact layer height to which the imported model can be evenly divided results in 40

Table 3

Area deviation (theoretical) converted into radius difference.

Test specimen	A (Cylinder)			B (Hemisphere)		
	PRUSASlicer	3DSlicer	Slicer2	PRUSASlicer	3DSlicer	Slicer2
Element 1 (base radius: 6.35 mm)						
Deviation area [ $\text{mm}^2$ ]	-3.19	-37.49	12.12	-7.64	-47.31	10.2
Deviation radius [mm]	-0.08	-1.02	0.30	-0.19	-1.32	0.25
Relative deviation [%]	-1.27	-16.09	4.67	-3.06	-20.85	3.95

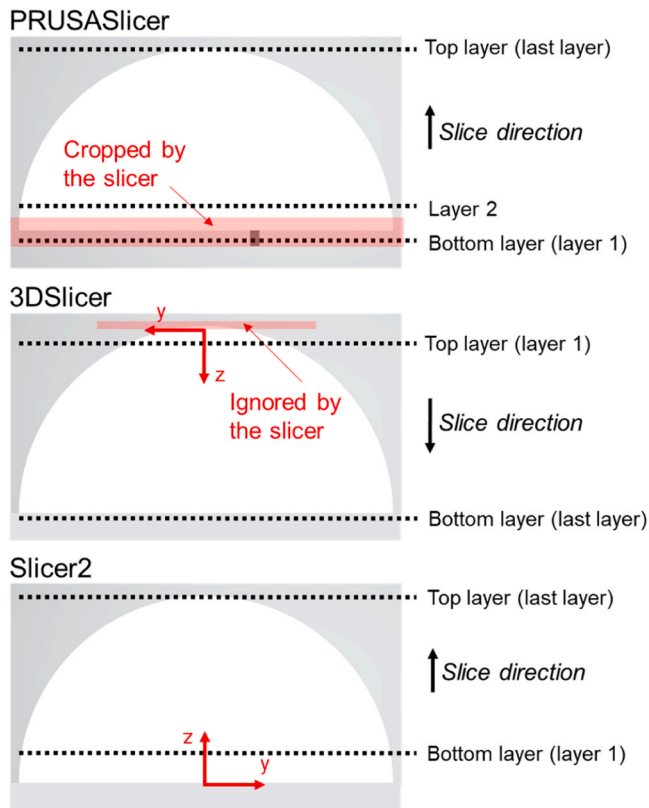


Fig. 17. Different slicing approaches of the three open-source slicers PRUSASlicer, 3DSlicer and Slicer2.

layers, but the circle in the last layer, barely recognizable, is composed of only 1 pixel. Adaptive slicing, that describes the strategy to adapt the slice interval to the curvature of the model (higher curvature requires lower slice interval), could reduce the staircase affect and improve the dimensional accuracy [65,66]. Omitting this last layer could also lead to a better shape of the printed result, as the 39th layer circle area is similar in size to the last layer obtained from the PRUSASlicer, which generated a specimen closest to the ideal shape.

The printed specimens based on the Creo assembly model are, compared to the corresponding part-based Creo model, slightly broader in the upper half of the hemisphere and flatter in the top region, which meets the ideal shape best. This observation aligns with the theoretical results for the assembly model that the dimensional deviation is almost zero. The surface profile of the printed assembly-based models generated from the image data obtained from the PRUSASlicer and the 3DSlicer is rather similar and contains less distinctive staircase effect, confirming that a precise STL model can compensate this effect.

## 5. Conclusion

The objective of the present study is to determine the impact of CAD design, CAD software, the usage of assembly vs part model, alternative 3D model formats and slicer software on the geometrical and dimensional accuracy of the generated print data in Material Jetting. Following findings can be concluded:

Each CAD software operates on a different tessellation algorithm, thus the achievable geometrical and dimensional accuracies vary for different CAD software programs. The targeted accuracy during tessellation is determined to be governed by the size of the individual elements in the model. For very small elements the dimensional deviation is mainly caused by the rasterization process, whereas for larger elements the accuracy of tessellation plays a significant role for the resulting dimensional accuracy of the print data.

For some CAD systems, e.g. Inventor, designing in assembly mode improves the accuracy compared to the part-based design, most likely due to the introduction of an additional error-reducing factor to the maximum tessellation deviation for small radii elements. No difference is obtained between these two design modes for some other design software, such as Solidworks, as it is assumed that this corrective factor for small radii is already applied to the part-based model. In other cases, Creo for instance, extended tessellation settings and value range in the assembly mode can be unlocked which allow more accurate 3D models to be exported.

Within the constraints of this study, the 3D formats 3MF and OBJ do not show any benefits in terms of less dimensional deviation compared to a STL model. The main advantage of using these alternative 3D model formats is the reduction of file size, with 3MF achieving the lowest size.

The AMF format is developed to include elements of curved triangular facets to approximate curved 3D objects more accurately. In this study, it is observed that not all CAD software exploit this capability of AMF. Additionally, some open-source slicers are unable to read the advanced AMF files containing elements with curved triangular facets.

The study confirms the influence of the slicer on the dimensional and, in particular, the geometrical accuracy of the slice images and printed part due to different approaches in handling the tessellated 3D model within the slicer. The direction of slicing can affect the geometrical outcome of the printed parts with heights that are not the multiple integer of the slice interval.

Moreover, some slicers remove certain regions of the imported object, either due to the misalignment of the model to the origin of the slicer's internal coordinate system or due to some process-specific reasons.

This study shows that the obtained sliced images derived from a slicer designed for Vat Photopolymerization technology can be utilized to generate print images for Material Jetting.

The printed specimens demonstrate that for a hemisphere surface, an equidistant slicing produces a very distinct sharp tip. As the slicing plane approaches the tip of the hemisphere, the difference in the sliced diameter between two subsequent layers increases, leading to a pronounced staircase effect.

For hemispherical elements, omitting the last layer (tip layer) results in a printed part that more closely resembles the ideal model.

For the printed specimens, it is observed that for the base layer the measured dimensional deviation exceeds the calculated deviation. This implies that the changes are obscured by printing-related factors, particularly by the wetting behavior between the substrate and the printed droplets. Nevertheless, the correlation between geometrical and dimensional deviation and working principles of CAD software, CAD model design and slicing approach can be detected.

Future studies should extend the investigation to the printing process-related deviation to obtain a complete picture of the dimensional and geometrical deviations in Material Jetting. In particular for multi-material printing, the induced geometrical and dimensional deviations for each material might vary in magnitude, as some responses are specific to the material's properties, such as shrinkage, warping, etc., necessitating a close control of the deviations.

Dissecting and quantifying the expected deviations for each step is fundamental for applying compensation measures to minimize the geometrical and dimensional deviation of the printed object. Proposing a mathematical formula to link the correlation between various tessellation parameters and accuracy would supply a valuable tool for AM operators in ensuring the same dimensional fidelity to be achieved when exchanging and exporting a STP model to a tessellated model. Furthermore, some printheads are capable of jetting droplets with different volumes by utilizing so-called grayscale waveform so that grayscale images can be printed for a better edge quality. In order to realize grayscale printing at this printer, the image could be first converted into multiple sub-images, each of them only containing pixels of the same grayscale level, so that these sub-images could be printed

either in separate successive print jobs or by multiple printheads, each of them deploying a different waveform. Advanced slicing strategy, such as adaptive layer height or the skipping/removal of layers in dependence on the geometry should be considered as well to improve the geometrical accuracy of the printed specimen.

## Funding

This work was carried out with the financial support of the Karlsruhe Nano Micro Facility (KNMF, [www.knmf.kit.edu](http://www.knmf.kit.edu)), a Helmholtz Research Infrastructure at Karlsruhe Institute of Technology (KIT, [www.kit.edu](http://www.kit.edu)) and under the Helmholtz Research Programme MSE (Materials Systems Engineering) at KIT.

## CRediT authorship contribution statement

**Steffen G. Scholz:** Writing – review & editing, Supervision, Conceptualization. **Ahmed Elkaseer:** Writing – review & editing, Formal analysis, Data curation. **Karin J. Chen:** Writing – review & editing, Writing – original draft, Visualization, Methodology, Investigation, Formal analysis, Conceptualization. **Veit Hagenmeyer:** Writing – review & editing, Supervision, Funding acquisition.

## Declaration of Competing Interest

The authors declare that they have no known competing financial interests or personal relationships that could have appeared to influence the work reported in this paper.

## Data availability

Data will be made available on request.

## Acknowledgement

The authors would like to thank Mahmoud Salem and Andreas Schmidt from KIT for developing and providing the slicers “Slicer2” and “3DSlicer” for this study. We acknowledge the support by the KIT-Publication Fund of the Karlsruhe Institute of Technology.

## Authors agreement

We the undersigned declare that this manuscript (manuscript ID: ADDMA-D-24-01785, titled “On the correlation between pre-processing workflow and dimensional accuracy of 3D printed parts in high-precision Material Jetting”) is original, has not been published before and is not currently being considered for publication elsewhere.

We confirm that the manuscript has been read and approved by all named authors and that there are no other persons who satisfied the criteria for authorship but are not listed. We further confirm that the order of authors listed in the manuscript has been approved by all of us.

We understand that the Corresponding Author is the sole contact for the Editorial process. He/she is responsible for communicating with the other authors about progress, submissions of revisions and final approval of proofs

## References

- [1] T.J.K. Buchner, et al., Vision-controlled jetting for composite systems and robots, *Nature* vol. 623 (7987) (2023) 522–530, <https://doi.org/10.1038/s41586-023-06684-3>.
- [2] M.A. Skylar-Scott, J. Mueller, C.W. Visser, J.A. Lewis, Voxellated soft matter via multimaterial multinozzle 3D printing, *Nature* vol. 575 (7782) (2019) 330–335, <https://doi.org/10.1038/s41586-019-1736-8>.
- [3] ISO/ASTM 52900:2021 Additive manufacturing — General principles — Fundamentals and vocabulary, International Standard Organization (ISO) 2021. [Online]. Available: <https://www.iso.org/obp/ui/en/#iso:std:iso-astm:52900:ed-2:v1:en>.
- [4] T. Han, S. Kundu, A. Nag, Y. Xu, 3D printed sensors for biomedical applications: a review, *Sensors* vol. 19 (7) (2019), <https://doi.org/10.3390/s19071706>.
- [5] H. Yuk, et al., 3D printing of conducting polymers, *Nat. Commun.* vol. 11 (1) (2020) 1604, <https://doi.org/10.1038/s41467-020-15316-7>.
- [6] M. Ali, F. Alam, H. Butt, Fabrication of 5D fresnel lenses via additive manufacturing, *ACS Mater. Au* vol. 2 (5) (2022) 602–613, <https://doi.org/10.1021/acsmaterialsau.2c00026>.
- [7] A. Lion, R.D. Wildman, M.R. Alexander, C.J. Roberts, Customisable tablet printing: the development of multimaterial hot melt inkjet 3D printing to produce complex and personalised dosage forms, *Pharmaceutics* vol. 13 (10) (2021), <https://doi.org/10.3390/pharmaceutics13101679>.
- [8] B. Chu, et al., Proangiogenic peptide nanofiber hydrogel/3D printed scaffold for dermal regeneration, *Chem. Eng. J.* vol. 424 (2021) 128146, <https://doi.org/10.1016/j.cej.2020.128146>.
- [9] G.L. Duffy, H. Liang, R.L. Williams, D.A. Wellings, K. Black, 3D Reactive Inkjet Printing of Poly-L-lysine/gellan Gum Hydrogels for Potential Corneal Constructs, in: *Materials science & engineering. C*, vol. 131, Materials for biological applications, 2021, <https://doi.org/10.1016/j.msec.2021.112476>.
- [10] R. Walczak, B. Kawa, K. Adamski, Inkjet 3D printed microfluidic device for growing seed root and stalk mechanical characterization, *Sens. Actuators A Phys.* vol. 297 (2019) 111557, <https://doi.org/10.1016/j.sna.2019.111557>.
- [11] A. Elkaseer, K.J. Chen, J.C. Janhsen, O. Refle, V. Hagenmeyer, S.G. Scholz, Material jetting for advanced applications: a state-of-the-art review, gaps and future directions, *Addit. Manuf.* vol. 60 (2022) 103270, <https://doi.org/10.1016/j.addma.2022.103270>.
- [12] T. Pirman, M. Oceppek, B. Likozar, Radical polymerization of acrylates, methacrylates, and styrene: biobased approaches, mechanism, kinetics, secondary reactions, and modeling, *Ind. Eng. Chem. Res.* vol. 60 (26) (2021) 9347–9367, <https://doi.org/10.1021/acs.iecr.1c01649>.
- [13] Mimaki Europe “3DUJ-553 The world’s first full-color 3D UV-curable inkjet printer.” <https://www.mimakieurope.com/products/3d/3duj-553/> (accessed May 19, 2023).
- [14] C. Beckwith, et al., Needle in a haystack: detecting subtle malicious edits to additive manufacturing G-code files, *IEEE Embed. Syst. Lett.* vol. 14 (3) (2022) 111–114, <https://doi.org/10.1109/les.2021.3129108>.
- [15] A.L. Marsan, V. Kumar, D. Dutta, M.J. Pratt, An Assessment of Data Requirements and Data Transfer Formats for Layered Manufacturing, National Institute of Standards and Technology, Gaithersburg, MD, 1998, <https://doi.org/10.6028/nist.ir.6216>.
- [16] D.B. Kim, P. Witherell, Y. Lu, S. Feng, Toward a digital thread and data package for metals-additive manufacturing, *Smart Sustain Manuf. Syst.* vol. 1 (1) (2017) 75–99, <https://doi.org/10.1520/SSMS20160003>.
- [17] W. Liu, L. Li, A.K. Kochhar, A method for assessing geometrical errors in layered manufacturing. Part 1: error interaction and transfer mechanisms, *Int. J. Adv. Manuf. Technol.* vol. 14 (9) (1998) 637–643, <https://doi.org/10.1007/bf01192283>.
- [18] W. Liu, L. Li, A.K. Kochhar, A method for assessing geometrical errors in layered manufacturing. Part 2: mathematical modelling and numerical evaluation, *Int. J. Adv. Manuf. Technol.* vol. 14 (9) (1998) 644–650, <https://doi.org/10.1007/bf01192284>.
- [19] J. Lyu, X. Yang, Y. Li, J. Tan, X. Liu, Effect of build angle on the dimensional accuracy of monolithic zirconia crowns fabricated with the nanoparticle jetting technique, *J. Prosthet. Dent.* vol. 130 (4) (2023), <https://doi.org/10.1016/j.prosdent.2023.07.025>.
- [20] J.M. Pinto, et al., Sensitivity analysis of geometric errors in additive manufacturing medical models, 328–34, *Med. Eng. Phys.* vol. 37 (3) (2015), <https://doi.org/10.1016/j.medengphy.2015.01.009>.
- [21] J. Bryła, A. Martowicz, Study on the importance of a slicer selection for the 3D printing process parameters via the investigation of G-code readings, *Machines* vol. 9 (8) (2021), <https://doi.org/10.3390/machines9080163>.
- [22] Y. Garashchenko, V. Fedorovich, Y. Ostroverkh, P. Dašić, M. Anđelković, H. Onalla, Statistical analysis of deviations from the correct shape of surface depending on product orientation in workspace of additive machine, *Machines* vol. 11 (3) (2023), <https://doi.org/10.3390/machines11030348>.
- [23] G. Moroni, W.P. Syam, S. Petrò, Towards early estimation of part accuracy in additive manufacturing, *Procedia CIRP* vol. 21 (2014) 300–305, <https://doi.org/10.1016/j.procir.2014.03.194>.
- [24] A. Boschetto, L. Bottini, Accuracy prediction in fused deposition modeling, *Int. J. Adv. Manuf. Technol.* vol. 73 (5–8) (2014) 913–928, <https://doi.org/10.1007/s00170-014-5886-4>.
- [25] D. Dimitrov, W. van Wijck, K. Schreve, N. de Beer, Investigating the achievable accuracy of three dimensional printing, *Rapid Prototyp. J.* vol. 12 (1) (2006) 42–52, <https://doi.org/10.1108/13552540610637264>.
- [26] J.R. Chen, et al., Three-dimensional printing accuracy analysis for medical applications across a wide variety of printers, *J. Med. Imaging* vol. 10 (2) (2023), <https://doi.org/10.1117/1.JMI.10.2.026501>.
- [27] M. Salmi, K.S. Paloheimo, J. Tuomi, J. Wolff, A. Makitie, Accuracy of medical models made by additive manufacturing (rapid manufacturing), 603–9, *J. Craniomaxillofac Surg.* vol. 41 (7) (2013), <https://doi.org/10.1016/j.jcms.2012.11.041>.
- [28] J. Yang, Multimaterial 3D printing technology (3D printing technology series). London, United Kingdom; San Diego, CA, United States; Cambridge, MA, United States; Oxford, United Kingdom: Academic Press, an imprint of Elsevier, 2021, pp. xiii, 217 pages.
- [29] D. Godec, A. Pilipović, T. Breski, *General Process Workflow in Additive Manufacturing*, in: D. Godec, J. Gonzalez-Gutierrez, A. Nordin, E. Pei, J. Ureña

- Alcázar (Eds.), *A Guide to Additive Manufacturing*, Springer International Publishing, Cham, 2022, pp. 45–57.
- [30] K. Kardel, A. Khoshkhou, A.L. Carrano, Design guidelines to mitigate distortion in material jetting specimens, *Rapid Prototyp. J.* vol. 27 (6) (2021) 1148–1160, <https://doi.org/10.1108/rpj-08-2020-0192>.
- [31] A. Khoshkhou, A.L. Carrano, D.M. Blerch, Effect of build orientation and part thickness on dimensional distortion in material jetting processes, *Rapid Prototyp. J.* vol. 24 (9) (2018) 1563–1571, <https://doi.org/10.1108/rpj-10-2017-0210>.
- [32] Protolabs Network "How to design parts for material jetting 3D printing." <https://www.hubs.com/knowledge-base/how-design-parts-material-jetting-3d-printing/> (accessed Jan 27, 2024).
- [33] S. Hällgren, L. Pejryd, J. Ekengren, 3D data export for additive manufacturing - improving geometric accuracy, *Procedia CIRP* vol. 50 (2016) 518–523, <https://doi.org/10.1016/j.procir.2016.05.046>.
- [34] N. Majca-Nowak, P. Pyrzanowski, The analysis of mechanical properties and geometric accuracy in specimens printed in material jetting technology, *Materials* vol. 16 (8) (2023), <https://doi.org/10.3390/ma16083014>.
- [35] A. Elkaseer, K.J. Chen, M. Kuchta, S.G. Scholz, On the quantitative assessment of the effect of multiple process parameters on the printed layer height in 3D inkjet printing, *Virtual Phys. Prototyp.* vol. 18 (1) (2023), <https://doi.org/10.1080/17452759.2023.2269898>.
- [36] K.J. Chen, A. Elkaseer, S.G. Scholz, A study on the effect of process parameters on feature resolution in 3D inkjet printing, presented at the World Congress on Micro and Nano Manufacturing (WCMNM), Evanston, USA, Sep 18–21, 2023.
- [37] H. Yousef, B.T. Harris, E.N. Elathamna, D. Morton, W.S. Lin, Effect of additive manufacturing process and storage condition on the dimensional accuracy and stability of 3D-printed dental casts, *J. Prosthet. Dent.* vol. 128 (5) (2022) 1041–1046, <https://doi.org/10.1016/j.prosdent.2021.02.028>.
- [38] A. Kumar, P. Kumar, R.K. Mittal, H. Singh, Chapter 6 - Printing file formats for additive manufacturing technologies, in: A. Kumar, R.K. Mittal, A. Haleem Eds. (Eds.), in *Advances in Additive Manufacturing*, Elsevier, 2023, pp. 87–102.
- [39] J. Yang, N. Li, J. Shi, W. Tang, G. Zhang, F. Zhang, Chapter 2 - Foundation of 3D printing and CAD file formats used in the industry, in: J. Yang, N. Li, J. Shi, W. Tang, G. Zhang, F. Zhang Eds. (Eds.), *Multimaterial 3D Printing Technology*, Academic Press, 2021, pp. 17–42.
- [40] 3MF Consortium "The File Format Optimized for 3D Printing." <https://3mf.io/> (accessed Mar 14, 2023).
- [41] PTC "About the 3D Manufacturing Format — 3MF." [https://support.ptc.com/help/creo/creo\\_pma/r9.0/usascii/index.html#page/data\\_exchange/interface/About\\_the\\_3MF\\_format.html](https://support.ptc.com/help/creo/creo_pma/r9.0/usascii/index.html#page/data_exchange/interface/About_the_3MF_format.html) (accessed Mar 14, 2023).
- [42] C. Tan. "Blender NURBS Modeling: Simply Explained." All3DP. <https://all3dp.com/2/blender-nurbs-modeling/> (accessed Sep 3, 2023).
- [43] A.R. Nassar and E.W. Reutzel, A proposed digital thread for additive manufacturing, presented at the 2013 International Solid Freeform Fabrication Symposium, Austin, USA, Aug 12–14, 2013.
- [44] *ISO/ASTM52915:2020 Specification for additive manufacturing file format (AMF) Version 1.2*, International Standard Organization (ISO) 2020. [Online]. Available: <https://www.iso.org/obp/ui/#iso:std:iso-astm:52915:ed-3:v1:en>.
- [45] *ISO 10303: Industrial automation systems and integration — Product data representation and exchange*, International Standard Organization (ISO) 2022. [Online]. Available: <https://www.iso.org/obp/ui/#iso:std:iso:10303:-1:ed-2:v1:en>.
- [46] Y. Qin, Q. Qi, P.J. Scott, X. Jiang, Status, comparison, and future of the representations of additive manufacturing data, *Comput. Aided Des.* vol. 111 (2019) 44–64, <https://doi.org/10.1016/j.cad.2019.02.004>.
- [47] J. Guo, F. Ding, X. Jia, D.-M. Yan, Automatic and high-quality surface mesh generation for CAD models, *Comput. Aided Des.* vol. 109 (2019) 49–59, <https://doi.org/10.1016/j.cad.2018.12.005>.
- [48] W. Lu, J. Liang, M. Ren, H. Wu, J. Zhang, J. Liu, Robust and fast CAD model tessellation for inspection, *IEEE Trans. Instrum. Meas.* vol. 71 (2022) 1–14, <https://doi.org/10.1109/tim.2022.3156988>.
- [49] J. Xue. *Integration of CAD/CAPP/CAM*, De Gruyter, Berlin, Boston, 2018.
- [50] R. Grabowski. "Spatial continues to expand on a 'kernel' of an idea." GRAPHICSPEAK. <https://gfxspeak.com/newswatch/spatial-continues-expand/> (accessed 4 Jul, 2024).
- [51] shapr3d "What is CAD: the technological foundations of CAD software." <https://www.shapr3d.com/blog/what-is-cad-the-technological-foundations-of-cad-software> (accessed 4 Jul, 2024).
- [52] Parasolid "Facet Mesh Generation." [http://www.q-solid.com/Parasolid\\_Docs/chapters/fd\\_chap.55.html](http://www.q-solid.com/Parasolid_Docs/chapters/fd_chap.55.html) (accessed 4 Jul, 2024).
- [53] NumPy "NumPy." <https://numpy.org/> (accessed Dec 01, 2023).
- [54] Pillow "Python PIL." <https://python-pillow.org/> (accessed Dec 01, 2023).
- [55] OpenCV "Releases." <https://opencv.org/releases/> (accessed Dec 01, 2023).
- [56] P.D. Lax, R.S. Phillips, The asymptotic distribution of lattice points in Euclidean and non-Euclidean spaces, *J. Funct. Anal.* vol. 46 (3) (1982) 280–350, [https://doi.org/10.1016/0022-1236\(82\)90050-7](https://doi.org/10.1016/0022-1236(82)90050-7).
- [57] PTC "Controlling the Quality of Export." [https://support.ptc.com/help/creo/creo\\_pma/r9.0/usascii/index.html#page/data\\_exchange/interface/Controlling\\_the\\_Quality\\_of\\_Export.html](https://support.ptc.com/help/creo/creo_pma/r9.0/usascii/index.html#page/data_exchange/interface/Controlling_the_Quality_of_Export.html) (accessed Oct 3, 2023).
- [58] M. Šljivic, A. Pavlovic, M. Krašnik, and J. Ilić, Comparing the accuracy of 3D slicer software in printed enduse parts, presented at the 9th International Scientific Conference - Research and Development of Mechanical Elements and Systems (IRMES 2019), Kragujevac, Serbia, Sep 5–7, 2019, 012082.
- [59] Y.K. Lai, Y.C. Chung, An efficient and high quality rasterization algorithm and architecture in 3D graphics systems. 2015 IEEE International Symposium on Circuits and Systems (ISCAS), Lisbon, Portugal, 2015, pp. 2537–2540, <https://doi.org/10.1109/ISCAS.2015.7169202>.
- [60] F.L. Gaol, Bresenham algorithm: implementation and analysis in raster shape, *J. Comput.* vol. 8 (1) (2013), <https://doi.org/10.4304/jcp.8.1.69-78>.
- [61] Z. Ibrahim, A. Rashid, A. Marhoon, An algorithm for Path planning with polygon obstacles avoidance based on the virtual circle tangents, *Iraqi J. Electr. Electron. Eng.* vol. 12 (2) (2016) 221–234, <https://doi.org/10.37917/ijeee.12.2.13>.
- [62] F. Liang, Y. Shi, Y. Yu, G. Liu, D. Wang, Theoretical analysis of FDM printing technology and experimental analysis based on low melting point soft materials, *IOP Conf. Ser. Mater. Sci. Eng.* vol. 452 (2018), <https://doi.org/10.1088/1757-899x/452/2/022111>.
- [63] H.Y. Park, B.J. Kang, D. Lee, J.H. Oh, Control of surface wettability for inkjet printing by combining hydrophobic coating and plasma treatment, *Thin Solid Films* vol. 546 (2013) 162–166, <https://doi.org/10.1016/j.tsf.2013.03.067>.
- [64] J. Yuan, C. Chen, D. Yao, G. Chen, 3D printing of oil paintings based on material jetting and its reduction of staircase effect, *Polymers* vol. 12 (11) (2020), <https://doi.org/10.3390/polym12112536>.
- [65] S. Sikder, H.A. Kishawy, A. Barari Effect of Adaptive Slicing on Surface Integrity in Additive Manufacturing, presented at the 34th Computers and Information in Engineering Conference, Buffalo, USA, Aug 17–20, 2014.
- [66] F. Wasserfall, N. Hendrich, J. Zhang Adaptive Slicing for the FDM Process Revisited, presented at the 13th IEEE Conference on Automation Science and Engineering (CASE), Xi'an, China, Aug 20–23, 2017.